MISREGISTRATION IN
ADAPTIVE OPTICS
SYSTEMS

THESIS

Nathan Engstrom, Captain, USAF

AFIT/GE/ENG/09-14

DEPARTMENT OF THE AIR FORCE
AIR UNIVERSITY

AIR FORCE INSTITUTE OF TECHNOLOGY

Wright-Patterson Air Force Base, Ohio

AFIT/GE/ENG/09-14

Misregistration in Adaptive Optics Systems

THESIS

Presented to the Faculty

Department of Electrical and Computer Engineering

Graduate School of Engineering and Management

Air Force Institute of Technology

Air University

Air Education and Training Command

In Partial Fulfillment of the Requirements for the

Degree of Master of Science in Electrical Engineering
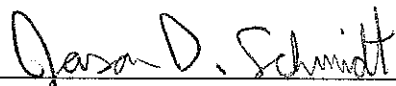
Nathan Engstrom, B.S.E.E.

Captain, USAF

March 2009

MISREGISTRATION IN
ADAPTIVE OPTICS
SYSTEMS

Nathan Engstrom, B.S.E.E.

Captain, USAF

Approved:

_____   _____
Maj J.D. Schmidt, PhD (Chairman)   date
                                                    06 Mar 09

_____   _____
Dr. S.J. Cusumano (Member)   date
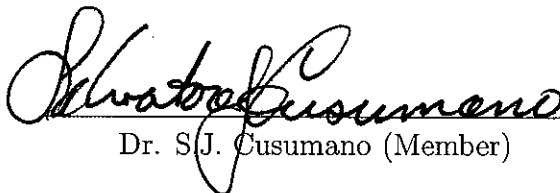   09 MAR 09

_____   _____
Lt Col G.J. Toussaint, PhD (Member)   date
                                                    06 MAR 2009

AFIT/GE/ENG/09-14

Abstract

An adaptive optics (AO) system is most effective when there is a known alignment between the wave front sensor (WFS) and the deformable mirror (DM). Misregistration is the term for the unknown alignment between the WFS and DM. Misregistration degrades system performance and can make the system unstable. An AO system uses a reconstruction matrix to transform WFS measurements into DM commands. A standard AO system uses a model reconstruction matrix that assumes perfect registration between the WFS and DM. The object of this research is to mitigate the negative effects of misregistration by using offline WFS measurements to create the reconstruction matrix. To build the reconstruction matrix, each actuator on the DM is poked to a fixed amount, and then the resulting measurement on the WFS is recorded. Analytic studies of the model and measured matrices show that the measured matrix yields a more stable AO system. Additional simulations indicate that applying the measured matrix improves the overall system performance compared to that of the model reconstruction matrix.

Table of Contents

List of Figures

List of Tables

List of Abbreviations

MISREGISTRATION IN

ADAPTIVE OPTICS

SYSTEMS

I. Introduction

This research was initiated by the Starfire Optical Range which is part of the Air Force Research Laboratory (AFRL), based in Kirtland AFB, NM. Since its construction in 2002, the mission of the Atmospheric Simulation and Adaptive optics (AO) Laboratory Testbed (ASALT) at AFRL is to provide research in the testing and development of advanced AO technologies and techniques [17]. The ASALT laboratory is currently studying misregistration. Setting up and maintaining a known, fixed optical alignment between an AO system's wavefront sensor (WFS) and deformable mirror (DM) is difficult. When the alignment between the WFS and DM is unknown or evolving, the AO system is said to have misregistration. Such misregistration degrades AO performance, and in some conditions, causes instability. Unfortunately, all AO systems have some degree of misregistration, even if it is small. Because of drift in optomechanical mounts and laboratory vibrations, minimizing misregistration requires highly trained engineers to constantly realign the system. For example, at the ASALT laboratory the AO system is aligned to within 3% of a subaperture. This requires much time and training.

This research focused on developing new mitigation strategies to reduce the negative effects of misregistration using techniques which require less training and more efficient set up procedures for the AO system. These strategies should be useful in vibration-sensitive environments that use AO, such as the Advanced Tactical Laser and Airborne Laser.

1

1.1 Problem Statement

The research objectives are to analyze misregistration within AO systems and to investigate mitigation strategies. The main mitigation strategy is to design a new reconstruction matrix (a transformation between the WFS measurements and DM commands) for the misaligned system by using the information measured by the WFS. The construction of this new reconstruction matrix was tested for both the Shack-Hartmann (SH) WFS and the self-referencing interferometer (SRI) WFS in numerical simulations. To further develop current techniques and new designs of building reconstruction matrices, analytical studies and simulations enable understanding of the AO system's stability. Monte Carlo simulations tested the impact of these reconstruction techniques on overall AO system performance.

1.2 Research Goals

This research used the so-called "poke" method to develop a reconstruction matrix that would be less sensitive to misregistration than an analytic reconstruction matrix. The poke method uses direct WFS measurements to build the reconstruction matrix. This was done by commanding each DM actuator to a fixed level and using the recorded WFS measurement to build the reconstruction matrix. In contrast, the traditional method of building the reconstruction method is to use a model to predetermine what the matrix should be. More specifically, the goals of this research are

- to analytically calculate stability bounds of the system with the SH WFS and using the new reconstruction matrix,

- to analytically calculate stability bounds of the system with the SRI WFS and using the new reconstruction matrix,

- to compare the performance of an AO system using a SH WFS with both the traditional reconstruction matrix and the new measured reconstruction matrix,

- to compare the performance of an AO system using a SRI WFS with both the traditional reconstruction matrix and the new measured reconstruction matrix, and

- to compare different analytic mitigation strategies with the measured reconstruction matrix.

Each of these goals was achieved. The analysis from this research showed that the new measured reconstruction matrix usually performs better than the analytic-model reconstruction matrix. The analysis shows that the measured matrix should maintain stability better than the model matrix in the presence of misregistration.

1.3 Thesis Overview

Chapter II gives an overview of some basic optics principles, the role of the atmosphere in optics, conventional AO, and the effects of misregistration in AO. The chapter begins with the Huygens-Fresnel principle used to calculate propagating optical fields. It continues with the turbulent nature of the atmosphere and discussion of how a wave is distorted when passing through the atmosphere. The next section explains the purpose of AO as well as the architecture of an AO system. The last section describes misregistration and its effects on the relevant system's stability. This information was used to illuminate current research in mitigating misregistration.

Chapter III introduces the means and methods that are used in performing the research. First it introduces the software package that was used to build and test each simulation. Next, it describes the exact methods used to build the reconstruction matrices and explores their attributes. Additionally, some of benefits, drawbacks, and uses of the different methods are discussed. Then, it outlines the different analytical calculations that needed to be accomplished to understand the stability of the system. Each analytical test and its individual benefits are described in detail. Finally, it outlines the various simulations that were used, including the specific atmospheric

conditions and AO settings of each simulation.

Chapter IV presents the analysis and results of the data taken from the simulations described in Chapter III. These results are presented in the form of plots representing loop transfer function poles, phase margins, stability boundaries, and Strehl ratios. These plots show improvements in the performance of the AO system and mitigation of instabilities, as well as limitations on the developed methods. This shows the need for further development of these techniques.

Chapter V contains final conclusions based on the results discussed in Chapter IV and discusses the benefits of the research. It also presents recommendations for future improvements to the process, including the use of different spatial filtering techniques.

II. Background

O ptics is the physics of light. Throughout history, man has studied light and how it propagates. Today, classical optics is divided into two main treatments: geometric optics and physical optics. Geometric optics describes the ray-like properties of light, approximating light propagation along a straight line, while physical optics describes the wave-like properties of light. This chapter discusses physical optics as well as some of the effects of the atmosphere and how it distorts light. It will also introduce AO and describe some details of its major components. Next, it will define misregistration and show its importance in AO systems. Finally, it will explain recently developed mitigation strategies and discuss their strengths and drawbacks.

2.1 Optics

Physical optics is based on the solutions of Maxwell's equations, which are considered the most fundamental starting point when studying electromagnetic waves. Physical optics treats light as an electromagnetic wave, and when a harmonic time dependence is assumed, the wave field (electric or magnetic) U can be written in phasor notation as $U = A \exp(j\phi)$, where A is the amplitude and ϕ is the phase. The study of physical optics has developed close ties with the communication and information disciplines of electrical engineering due to the similar nature of the mathematics used to describe the respective systems of interest. Because Maxwell's equations are linear, its solutions can be studied using linear systems theory and Fourier analysis. The two-dimensional Fourier transform operation of a function g with two independent variables x and y is given by:

$$\mathcal{F}\{g\} = \iint\limits_{-\infty}^{\infty} g(x,y) \exp[-j2\pi(f_X x + f_Y y)]dxdy, \qquad (2.1)$$

where f_X and f_Y are two independent variables that define the transform, generally representing spatial frequencies. This gives a starting point from which to describe

the characteristics and propagation of light.

Diffraction, the action that occurs when a wave encounters an obstacle, can be observed through the apparent bending of waves around small objects or the spreading of the wave as it passes through small openings. When studying diffraction, it is important to understand the Huygens-Fresnel principle, a consequence of Maxwell's equations. The Huygens-Fresnel principle states that every unobstructed point of a wavefront at a given instant serves as a source of spherical secondary wavelets (with the same frequency as that of the primary wave). The amplitude of the optical field at any point beyond is the superposition of all these wavelets (considering their amplitudes and relative phases) [8]. Based on this principle and Maxwell's equations, the Fresnel-Kirchhoff diffraction formula was developed as

$$U(P_0) = \frac{A}{j\lambda} \int\limits_{\Sigma_0} \frac{\exp[jk(r_{21} + r_{01})]}{r_{21}r_{01}} \left[\frac{\cos(\mathbf{S}, \mathbf{r}_{01}) - \cos(\mathbf{S}, \mathbf{r}_{21})}{2} \right] ds. \qquad (2.2)$$

This formula quantifies the phasor portion of any scalar electric or magnetic field component at an observation point P_0 behind an opaque planar screen with a transparent aperture defined by Σ_0 when the screen is illuminated by a point source of light [6]. In Eq. (2.2), A is the amplitude of the source, $\mathbf{r}_{21}$ is the distance from the source to the aperture, $\mathbf{r}_{01}$ is the distance from the aperture to the observation point, and $\mathbf{S}$ is the outward normal vector to the screen. These relationships are shown in Fig. 2.1.

The two major approximations from the Fresnel-Kirchhoff diffraction formula are used to reduce the diffraction pattern calculations to comparatively simple mathematical manipulations. The Fresnel and Fraunhofer approximations are used in many calculations that determine field values after wave propagation. This research used the Fresnel approximation to determine the field values.
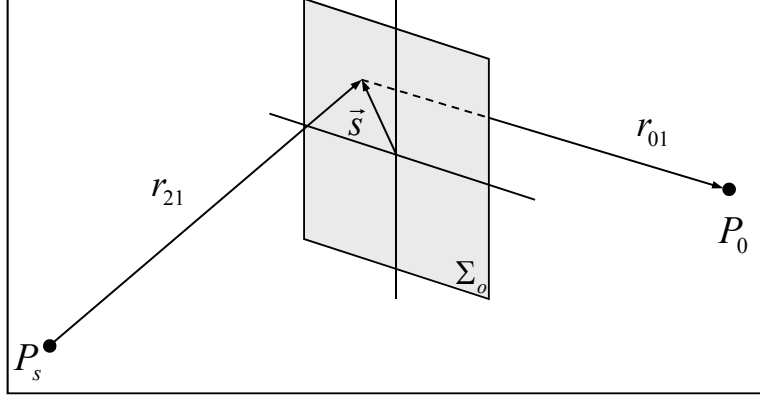
Figure 2.1: Fresnel-Kirchhoff diffraction area. The characterization of the electric field at P_0 given a point source, P_s. The summation of electric field takes place over the whole aperture. The field is based on the amplitude of the source and the distance from the aperture.

The Fresnel approximation, also called the near-field approximation because it is valid for both short and long propagation distances, is fully covered in Ref. [6]. It is:

$$U(x,y) = \frac{e^{jkz}e^{j\frac{k}{2z}(x^2+y^2)}}{j\lambda z} \int\limits_{-\infty}^{\infty}\!\!\!\int U(\xi,\eta)e^{j\frac{k}{2z}(\xi^2+\eta^2)}e^{-j\frac{2\pi}{\lambda z}(x\xi+y\eta)}d\xi d\eta. \tag{2.3}$$

This is used to calculate the field across the observation (x, y) plane, which is parallel to the source (ξ, η) plane and at a normal distance z from it. The Fourier transform, defined in Eq. (2.1) can be used to evaluate Eq. (2.3) efficiently in a computer [14]. This is the basis of the simulations discussed later.

2.2 Atmosphere

The effects of Earth's atmosphere are clearly apparent in the perceived twinkling of the stars. The three primary atmospheric phenomena that affect optical wave propagation are absorption, scattering, and refractive-index fluctuations (i.e., optical turbulence) [1]. Optical turbulence is caused by inhomogeneities that occur in the atmospheric refractive index due to the heating and cooling of the Earth which leads to
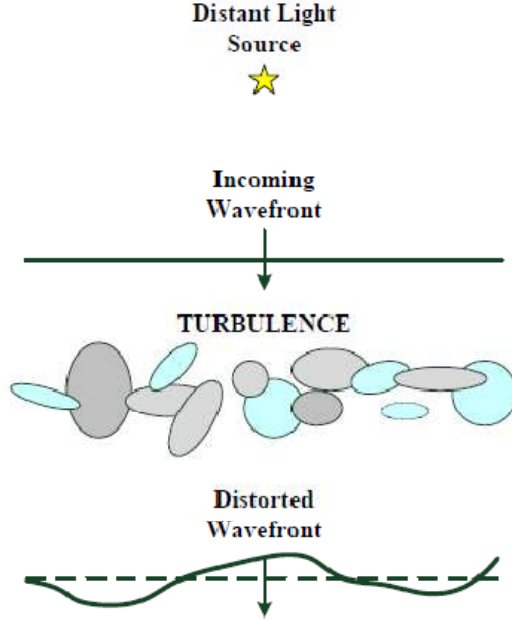
Figure 2.2: Wavefront distortion due to turbulence. The incoming wavefront enters the atmosphere and is distorted by turbulence. The image is courtesy of Ref. [17] .

turbulent air flow in the free atmosphere [17]. These inhomogeneities naturally break down into smaller inhomogeneities by the movement of the air. This is a natural random process that causes turbulent wind motion, forming eddies or small pockets of similar air. Each eddy refracts the light as it propagates through the atmosphere, causing the original wavefront to be distorted, as shown in Fig. 2.2. The result of this distortion in imaging is a randomly evolving blur, hence the twinkling of the stars.

Turbulence distorts phase more severely than amplitude, especially for ground-based telescopes pointed upward. Further, phase distortions at the entrance pupil of an imaging system have a greater impact on image quality than do amplitude distortions. Consequently, this discussion focuses primarily on optical phase.

Often, the undistorted field is a plane wave. An ideal plane wave is expressed by

$$U(x,y,z) = Ae^{j\frac{2\pi}{\lambda}(\alpha x + \beta y)}e^{j\frac{2\pi}{\lambda}\gamma z}, \tag{2.4}$$

where

$$\gamma = \sqrt{1 - \alpha^2 - \beta^2} \tag{2.5}$$

and

$$\alpha = \lambda f_X \tag{2.6}$$

$$\beta = \lambda f_Y. \tag{2.7}$$

This wave is represented more compactly as $U(x,y,z) = A\exp[j\phi^{ideal}(x,y,z)]$. As this wave passes through the atmosphere's turbulence, the phase becomes distorted. The atmospheric turbulence is represented by adding an additional term to the phase which results in an equation for the distorted wavefront:

$$U = A\exp[j(\phi^{ideal}(x,y,z) + \phi^{turb}(x,y,z))]. \tag{2.8}$$

Because the atmosphere's refractive index is a random field, dependent on location and time, a model of refractive-index variations must be used to determine properties of the distorted phase. A power spectral density (PSD) can represent the index of refraction fluctuations caused by the numerous eddies in the atmosphere. The PSD is represented by $\Phi_n(\kappa)$, where κ is the angular spatial frequency (measured in rad/m) and is composed of κ_x, κ_y, and κ_z which are the cartesian components. The fluctuations are assumed to be locally homogeneous and spatially isotropic, which means that statistical moments of n_1 are invariant to translation and rotation [17].

A variety of mathematical models represent $\Phi_n(\kappa)$. The Kolmogorov model accurately represents $\Phi_n(\kappa)$ in a certain range of spatial frequencies, which is defined by the sizes of the turbulent eddies. The region is defined by the inner scale l_0 and the

9

outer scale L_0. The inner scale represents the smallest size of turbulent eddies, and the outer scale represents the largest size of turbulent eddies. For the region where $2\pi/L_0 \leq \kappa \leq 2\pi/l_0$, the Kolmogorov model is shown by

$$\Phi_n^K(\kappa) = 0.033 C_n^2 \kappa^{-11/3} \ , \tag{2.9}$$

where C_n^2 is the structure parameter of the fluctuations of the index of refraction and is in units of $\text{m}^{-2/3}$. Outside these bounds, the Kolmogorov model can no longer match the spatial PSD of the index of refraction. The structure parameter is a function of altitude and varies with time of day and geographic location. Consequently, there are many different models that represent C_n^2 for different locations and in other conditions.

When the Kolmogorov power spectrum is used with the Rytov approximation for solutions to Maxwell's equations in the presence of turbulence, correlation properties of the distorted phase are obtained [1]. There are two important phase correlation parameters relevant to this research. These are the coherence diameter, which is a measure of spatial correlation, and the Greenwood frequency, which is a measure of temporal correlation.

The atmospheric coherence width, or Fried parameter, indicates the spatial scale of turbulence at a particular location. This parameter impacts the performance of an imaging system. The Fried parameter indicates the largest telescope diameter at which resolution no longer improves and is given by [1]

$$r_0 = \left[0.42 k^2 \sec \zeta \int_0^L C_n^2(z) dz \right]^{-3/5} \tag{2.10}$$

for a plane wave, where $k = 2\pi/\lambda$, ζ is the zenith angle, and C_n^2 is integrated over the entire propagation path coordinate z. Typical values of r_0 are 5-10 cm for a ground-based telescope at sea level observing visible light directly overhead.

The characteristic temporal correlation interval of the atmosphere, called the Greenwood time constant τ_0, is used to identify the interval over which turbulence remains statistically unchanged. The closely related Greenwood frequency is given by

$$f_G = \frac{1}{\tau_0} = \left[2.91 k^2 \int_0^L C_n^2(z) V_\perp^{5/3}(z) dz \right]^{3/5}, \qquad (2.11)$$

where $V_\perp(z)$ is the transverse wind velocity as a function of propagation distance. [1] For a constant wind speed $V_\perp$, f_G can be directly related to Fried's parameter by

$$f_G = 0.436 \frac{V_\perp}{r_0}. \qquad (2.12)$$

The Greenwood frequency is normally in the range of 20 to 200 Hz.

The Strehl ratio is a measure of performance of an imaging system. The Strehl ratio is defined by the ratio of the peak focal-plane mean irradiance in the presence of atmospheric turbulence to the peak focal-plane free-space irradiance [1]. When turbulence is present, the system's phase variance is a composed of the high-order variance and tilt variance whose sum is given by

$$\sigma_\phi^2 \approx 1.029 \left(\frac{D}{r_0} \right)^{5/3}, \qquad (2.13)$$

where σ_ϕ^2 is the system's phase variance. The system phase variance is used in determining the Strehl ratio

$$SR \approx \exp(-\sigma_\phi^2). \qquad (2.14)$$

Adaptive optics systems (discussed below) seek to improve image quality by reducing these phase variations in real time.

2.3 Adaptive Optics

AO is a class of technologies that compensate for the phase distortion introduced by the atmosphere in real time. The AO system seeks to flatten the phase to provide compensation for phase distortion [16]. A simple AO system is depicted in Fig. 2.3. The three major components of an AO system include the WFS, the DM, and the control computer. The WFS senses the shape of the incoming wavefronts or wavefront gradients that are transformed by the control computer in DM commands. The DM reshapes itself to the conjugate of the distorted wavefront to compensate for the distortion added to the wavefront by the atmosphere. The control computer serves as the transformation between the WFS measurements and the DM commands.

2.3.1 Wavefront Sensors.   The wavefront sensor acts as the eyes of the system, however the technology does not yet exist to measure the phase of the field directly. Consequently, different methods have been developed to indirectly measure the phase. The square of the amplitude, irradiance, is easily measured and is used to infer optical phase or its gradient. The phase can be measured in a few different ways. The SH WFS measures the gradients of the field, while the SRI uses an interference properties of waves to measure the wavefront.

2.3.1.1 Shack-Hartmann Wavefront Sensor.   SH WFSs are the most commonly used WFS in traditional AO systems. A SH WFS, shown in Fig. 2.4, consists of a lenslet array followed by a focal plane sensor array, which acts as an array of quad cells [9]. An example of one such WFS focal plane array element (quad cell) is shown in the upper right hand corner of Fig. 2.4. The tilt, or gradient, of each quad cell in the WFS focal plane array is determined using

$$S_x = \frac{(I_a + I_d) - (I_b + I_c)}{(I_a + I_b + I_c + I_d)} \tag{2.15}$$

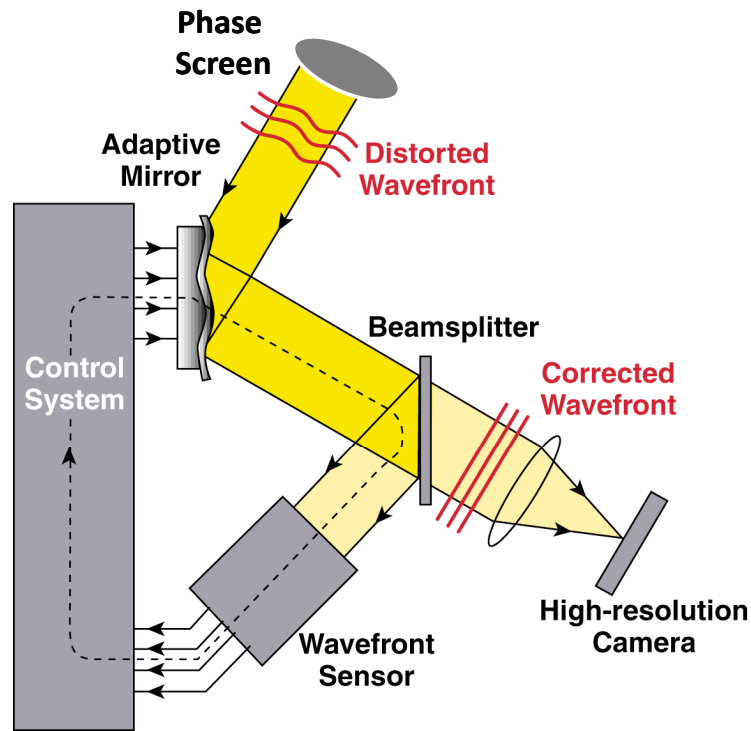Figure 2.3: AO simulation system where the light enters through the phase screen and is then reflected off the DM. The wavefront is then split as a portion goes to a high-resolution camera and the other part continues onto the WFS. The WFS relays the information to the control computer which maps the signals into commands for the DM. The image is courtesy of Dr. Claire Max at the Center for Adaptive Optics.
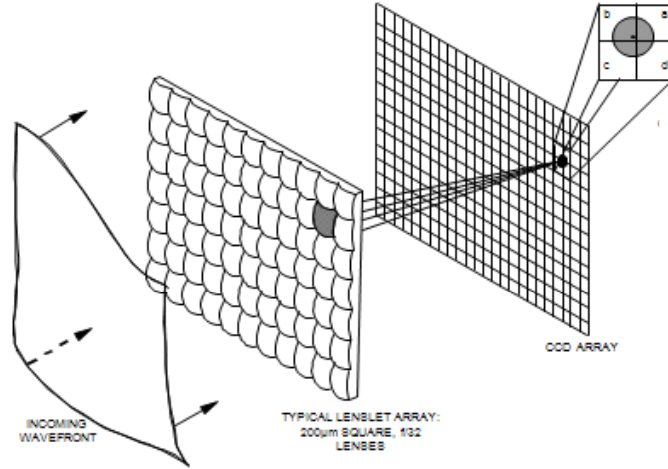
Figure 2.4: Shack-Hartmann WFS is shown where the incoming wavefront encounters a lenslet array that focuses it onto a sensor. The sensor the produces the local gradient of the cell. The image is courtesy of Ref. [15].

$$S_y = \frac{(I_a + I_b) - (I_c + I_d)}{(I_a + I_b + I_c + I_d)}, \tag{2.16}$$

where S_x and S_y are the gradients in the x and y directions, respectively, and I_a, I_b, I_c, and I_d are the intensities of the spot measured in quadrants a, b, c, and d, respectively. The process by which gradients are transformed into phase is called wavefront reconstruction. This process involves applying the inverse of the geometry matrix to a vector of wavefront gradients [9].

The geometry matrix Γ maps a vector of actuator commands to a vector of subaperture measurements [2]. In order to find the geometry matrix, the WFS-DM geometry must be known. For this research the SH WFS uses Fried geometry (see Fig. 2.6 for an example). The geometry matrix is a $n \times m$ matrix in which the n columns represent the actuators of the DM and m rows show the x and y slopes. For the Fried geometry, these slopes are measured at the center of each subaperture. In Fig. 2.6, each square represents a WFS subaperture (and individual quad cell in the WFS array); x and y wavefront gradients correspond to each subaperture. In the example shown in Fig. 2.5, $n = 9$ and $m = 8$. For the Fried geometry, the reconstruction matrix takes
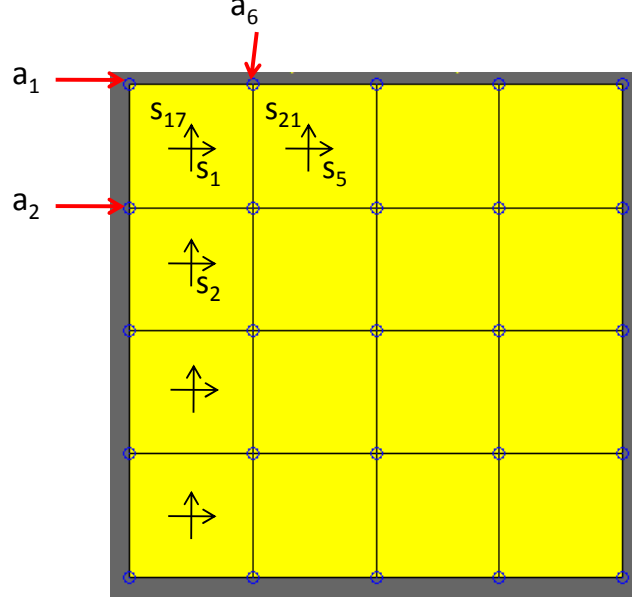
Figure 2.5:   DM numbering convention for the geometry matrix.

the form

$$(s_x)_{n,m} = \frac{1}{2}(\phi_{n+1,m} - \phi_{n,m}) + \frac{1}{2}(\phi_{n+1,m+1} - \phi_{n,m+1})$$

$$(s_y)_{n,m} = \frac{1}{2}(\phi_{n,m+1} - \phi_{n,m}) + \frac{1}{2}(\phi_{n+1,m+1} - \phi_{n+1,m}), \qquad (2.17)$$

where $\phi_{n,m}$ are the phases shown in the Fig. 2.6. The two-dimensional phase values are reshaped into a column-major ordering to create a one-dimensional vector. The same is done with the slopes. Typically in the slope vector, the s_x values are inserted into the first half of the slope vector, while the s_y values are inserted into the second half of the slope vector. With this ordering, the Fried-geometry system of equations can be written more compactly as:

$$\mathbf{s} = \Gamma\phi. \qquad (2.18)$$

The system of equations is over-determined, and so the least-queares solution for the phase vector uses the *Moore-Penrose pseudo-inverse* with the property $H\Gamma = I$,

15
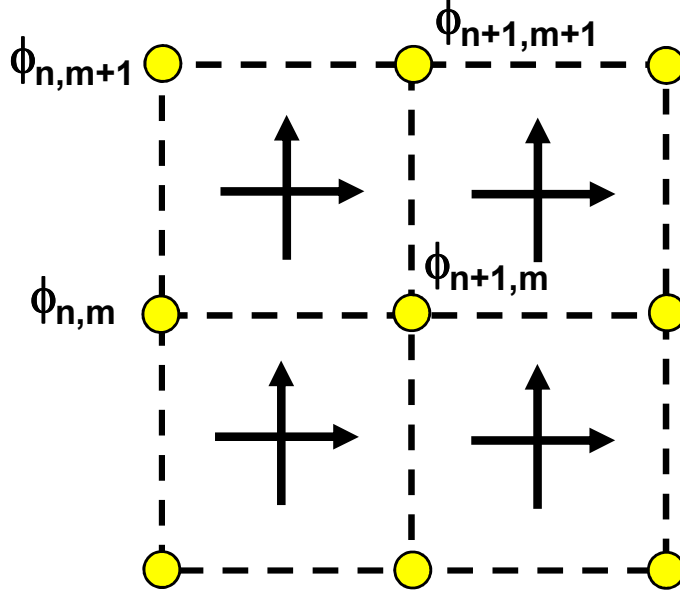
Figure 2.6: Fried geometry of Shack-Hartmann WFS. The local gradients are measured at the center of the each subaperture by using Eq. (2.17). The image is courtesy of Ref. [15].

where I is the identity matrix, so that [11]

$$\phi = (\Gamma^T\Gamma)^{-1}\Gamma^T\mathbf{s}. \tag{2.19}$$

The matrix $\Gamma^T\Gamma$ is singular if any null modes exist. The rank deficiency of $\Gamma^T\Gamma$ is equal to the dimension of the null space of Γ. The Fried geometry, for example, has two null modes: two orthogonal types of waffle. In this case, the rank deficiency of Γ is two, and thus the solution to Eq. (2.19) is not explicitly defined via the pseudo-inverse [5]. With $\mathbf{s}$ being the vector of measured slopes, then the least-squares problem is to find the vector of actuator commands $\mathbf{a}$ that minimizes the square residual error

$$E^2 = |\mathbf{s} - \Gamma\mathbf{a}|^2. \tag{2.20}$$

2.3.1.2 Self-Referencing Interferometer Wavefront Sensor. In contrast with the Shack-Hartmann WFS, which measures the gradients, the SRI WFS

16

directly measures the wavefront. The SRI WFS is based on a phase-shifting, point diffraction interferometer [12]. The basic design of the SRI is such that the incoming beam splits in two separate parts: a reference beam and a beacon beam. The reference beam couples into a single-mode fiber that spatially filters the beam, resulting in a known field at the output of the fiber. The beacon beam travels the same distance and combines with the known field at a WFS camera, where together they produce interferometric fringes. The SRI WFS measures the average field over each subaperture, and estimates of the amplitude, $\hat{A}_b(x_m, y_m)$, and phase, $\hat{\phi}_b(x_m, y_m)$, of the beacon field can be found from

$$\hat{A}_b(x_m, y_m) = \frac{1}{4\mathcal{A}_m}\sqrt{[I_1(x_m, y_m) - I_3(x_m, y_m)]^2 + [I_4(x_m, y_m) - I_2(x_m, y_m)]^2} \quad (2.21)$$

$$\hat{\phi}_b(x_m, y_m) = \arg\left\{\hat{U}(x_m, y_m)\right\} = \arctan\left(\frac{I_4(x_m, y_m) - I_2(x_m, y_m)}{I_1(x_m, y_m) - I_3(x_m, y_m)}\right), \quad (2.22)$$

where the results of the arctangent are between $-\pi$ and π. For Eqs. (2.21) and (2.22) $I_n(x_m, y_m)$ is the intensity measured for the nth phase shift in m^{th} subaperture of the SRI WFS, using a set of phase shifts of $[0, \pi/2, \pi, 3\pi/2]$. Also, $\mathcal{A}_m$ is the subaperture area. Figure 2.7 shows a diagram of the SRI WFS. Analysis has shown that the ability of the SRI WFS to estimate the beacon field depends only on the ratio of the subaperture size to the atmospheric coherence length [12].

Two ways to accomplish these phase shifts are spatial phase shifting and temporal phase shifting. Spatial phase shifting allows all four measurements to be captured simultaneously. To accomplish spatial phase shifting, the reference and beacon beams are each split into four beams, and the proper phase shift is applied with static waveplates. The fringe patterns are then measured on either four different detectors or four separate regions of a single detector. Temporal phase shifting is accomplished by adding the phase shift temporally into the fiber using a fiber phase shifter. A single detector array is used to capture the images sequentially in four integration cycles.

17
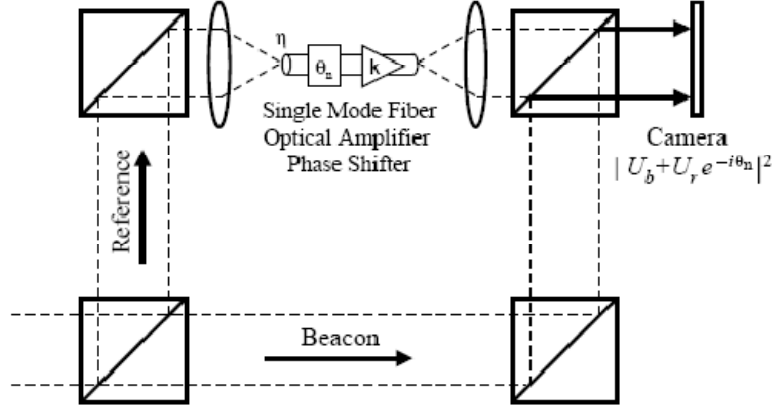
Figure 2.7: Diagram of the SRI WFS. The wavefront enters the system at the bottom left hand corner and is divided into a reference beam and beacon beam. The reference beam is focused into a single mode fiber which adds a phase shift onto the beam. The beams are allows to interfere with each other and produce interference patterns that can be measured. Image courtesy of [12].

Each method has its drawbacks and strengths.

The spatial method ensures the use of the same signal and reference wavefronts for all the interference measurements, effectively freezing the atmosphere [13]. However, it also requires a more complex hardware design and increases overall system size and cost. The ASALT laboratory has designed a spatial phase shifting SRI WFS shown in Fig. 2.8 [13]. Other potentially problematic areas of that the spatial method include co-aligning the beams, achieving accurate calibration across all detectors, and non-common path aberrations.

With the temporal method, the dynamic nature of the atmospheric turbulence is cause for concern. The field within each subaperture changes with time. Consequently, the phase and amplitude of the signal wave are different in each measurement. Additionally, the phase and amplitude of the reference also drift with time, independent of the phase shift introduced by the fiber phase shifter [13]. In order to maintain a Strehl ratio of 0.9 or higher, the sample rate of the SRI WFS must be at least a
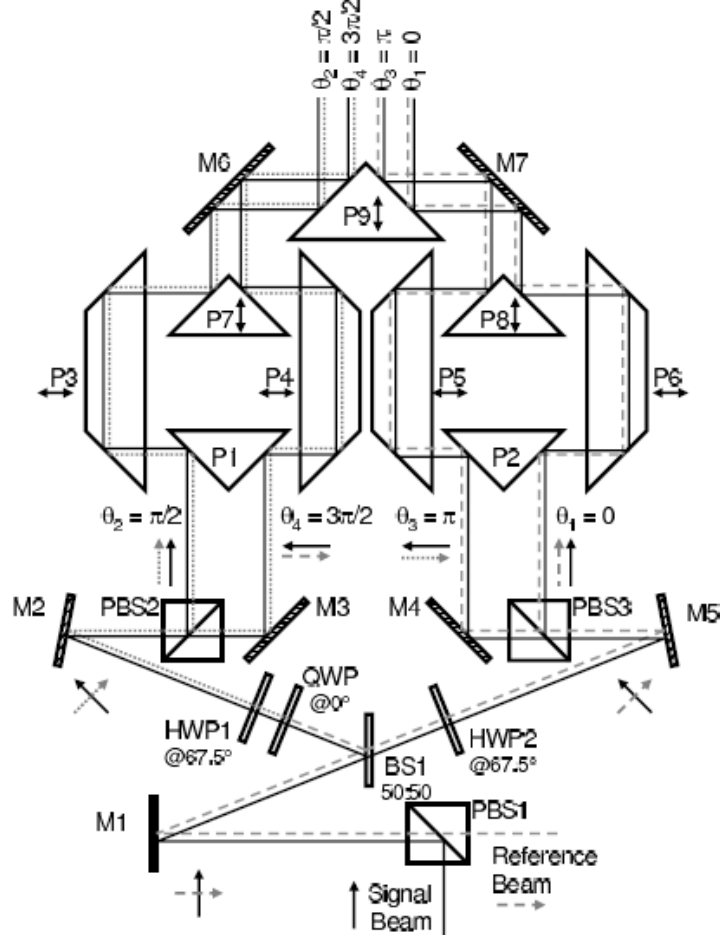
Figure 2.8:   Design of a spatial phase shifting SRI WFS. The reference beam paths are denoted by the solid black lines. The paths for the beacon beam are denoted by the dashed gray lines. The finely dotted gray lines indicate that the reference has been delayed by $\pi/2$. The arrows to the sides of the beam paths indicate the polarizations of the signal and reference beams at different positions in the system. This image is courtesy of Ref. [13].

19

100 times that of the Tyler frequency (characteristic frequency of atmospheric tilt, similar to Greenwood frequency) for an aperture the size of a WFS subaperture [12]. Furthermore, the fiber phase shifter may not always give the desired consistent phase shift due to hysteresis or other issues with the device.

The wavefront measurements can be used to control a DM in an AO system, however the output of Eq. (2.22) is limited to the range $-\pi < \hat{\phi}_b \le \pi$. Though this is not a problem for a segmented DM, the wavefront must be unwrapped for a continuous-surface DM. There are many different methods of unwrapping the phase. One simple method for unwrapping the phase is a least-squares unwrapping algorithm. This method has a finite and defined number of calculations and is similar to conventional AO phase reconstruction.

In order to unwrap the phases, the slopes are found and then a geometry matrix reconstructs the slopes into unwrapped phase. The SRI uses the Hudgin reconstruction geometry, as seen in Fig. 2.9, in contrast to the Fried geometry that is used for the SH WFS. The Hudgin geometry matrix is a $n \times m$ matrix, in which the n columns represent the actuators of the DM and m rows show the x and y slopes. The slopes are measured directly between actuators; between adjacent horizontal actuators for the x slopes, and between adjacent vertical actuators for y slopes. In the example shown in Fig. 2.9, $n = 9$ and $m = 12$. For the Hudgin reconstruction geometry the reconstruction system of equations takes the following form:

$$
\begin{aligned}
(s_x)_{n,m} &= \phi_{n+1,m} - \phi_{n,m} \\
(s_y)_{n,m} &= \phi_{n,m+1} - \phi_{n,m}.
\end{aligned}
\tag{2.23}
$$

Using the same column-major ordering, as with the Fried geometry, Eq. (2.23) can be written more compactly as

$$
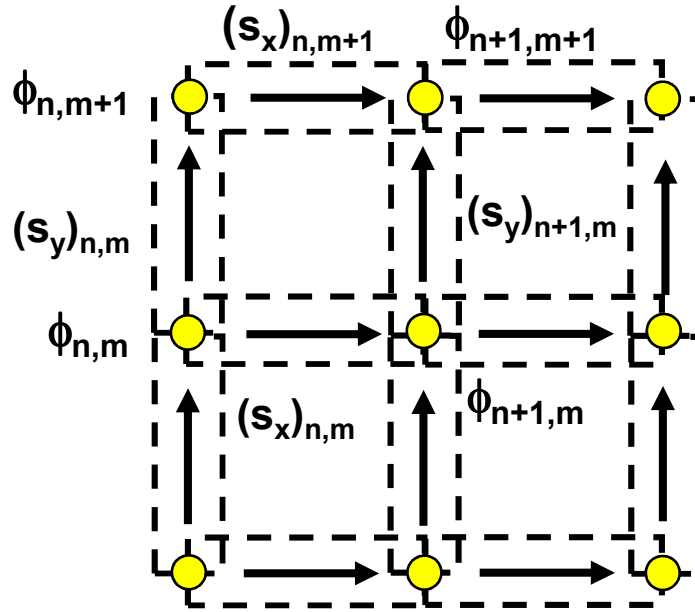\mathbf{s} = \Gamma \phi.
\tag{2.24}
$$

20

Figure 2.9:   Hudgin geometry used in the SRI reconstruction matrix. The Hudgin geometry measures the local gradients on the edges of the subaperture as shown in Eq. (2.23). This image is courtesy of Ref. [15].

This is identical to Eq. (2.18), but now Γ is the Hudgin geometry matrix. Solving for phases,

$$\phi = (\Gamma^T \Gamma)^{-1} \Gamma^T \mathbf{s}. \tag{2.25}$$

With this type of reconstruction geometry, there is only one mode in the null space of the matrix. The effects of misregistration on an AO system that uses an SRI WFS have not been researched until now.

2.3.2 Deformable Mirror. The DM can be considered the "hands" of an AO system, as it is the physically active object in the system. It has the ability to dynamically change its surface to correct the incoming wavefront. If an incident aberrated optical field represented by $A \exp[j\phi(\mathbf{x}, t)]$ is reflected off the surface of the DM, the resulting residual wavefront after reflection $A \exp[j\varepsilon(\mathbf{x}, t)]$ is given by [17]

$$
\begin{aligned}
A \exp[j\varepsilon(\mathbf{x}, t)] &= A \exp[j\phi(\mathbf{x}, t)] \exp[-j\hat{\phi}(\mathbf{x}, t)], \\
&= A \exp\{j[\phi(\mathbf{x}, t) - \hat{\phi}(\mathbf{x}, t)]\}.
\end{aligned}
\tag{2.26}
$$

In Eq. (2.27) t is time, $\phi(\mathbf{x}, t)$ is the piston-removed perturbed wavefront phase, $\hat{\phi}(\mathbf{x}, t)$ is the piston removed surface of the DM, and $\varepsilon(\mathbf{x}, t)$ is the residual phase of the wavefront after reflection. The DM's goal is to exactly conjugate aberrated wavefronts so that the residual phase is zero. There are many reasons why it is improbable that a DM can exactly conjugate an aberrated wavefront. For example, the physical properties of the DM limit how closely it can match the conjugate of a wavefront. While a high number of actuators allow a closer match to the wavefront, it will also increase the complexity of the system.

DMs are divided into two main categories, segmented and continuous, based on the type of reflective surface the DM has. Figure 2.10 shows these two classes of
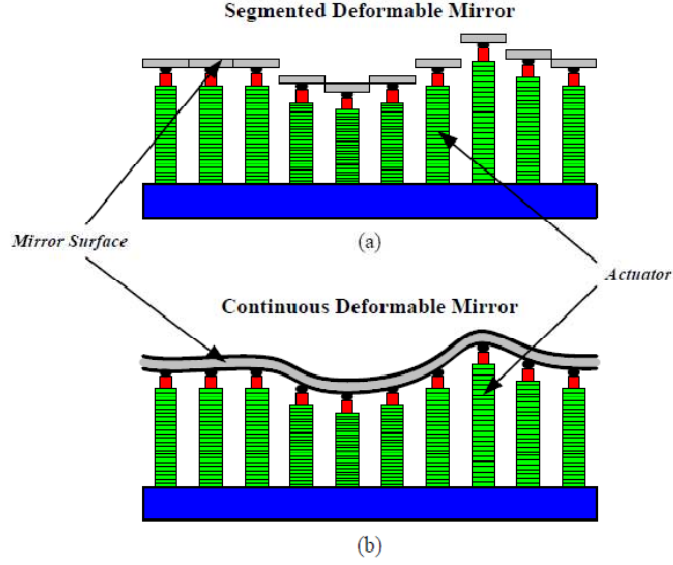
Figure 2.10: Continuous and segmented DMs. (a) Cross-section of a segmented face plated DM. (b) Cross-section of a continuous face plated DM. Image courtesy of Ref. [17].

DMs. Only continuous DMs are modeled in this research.

Segmented DMs have simplistic components, and are made of independently controlled segments which allows a greater degree of freedom of control. This freedom allows for simpler control laws, because a command given to one actuator has no influence on neighboring actuators. The components' simplicity means that all the segments are identical, so if one fails it can be replaced with relative ease. The disadvantages of a segmented DM are alignment and diffraction. Because each segment is independent of its neighbor, they must each be strictly aligned in both piston and tilt. Also, diffraction plagues segmented DMs, because no matter how close together the segments are, they require some space to move freely. This necessary space acts as an amplitude grating on the mirror.

Continuous DMs are constructed on one thin reflective sheet that is attached to the actuators. These actuators push and pull the face sheet to deform it. The face

sheet needs to be flexible enough to quickly adjust to actuators, but strong enough to resist wild deformation. Continuous DMs do not have the problem of diffraction because there are no gaps. However, this creates greater complexity in the control law due to the influence one actuator has on another. This coupling of actuators introduces a new factor called the influence function, or the amount of slope that is introduced in neighboring subapertures by pushing one actuator. Repairs on a continuous DM are much harder than on a segmented DM, because the actuators are coupled together and not independent.

The actuator spacing of the DM is important because it limits how much of the turbulence the DM can correct. This is characterized by the fitting error. The fitting error, which has the constant $a_F = 0.28$ for continuous facesheet DM's, is given by [7]

$$\sigma_{fit}^2 = a_F \left(\frac{d}{r_0} \right)^{5/3}. \tag{2.27}$$

This represents the residual phase variance due to the finite DM resolution. For segmented DMs, $a_F = 1.26$, so they require many more actuators to achieve the same performances as continuous DMs.

2.3.3 Control Law.   For the control computer to give the correct commands to the DM, a linear relationship is assumed between the actuator commands and sensor measurements. This is done by using the geometry matrix Γ, which is dependent on the type of WFS. The AO system is a closed-loop system, so after the system applies a correction, it then senses the consequence of that correction as shown in Fig. 2.3.

The common control law in AO is a proportional-integral (PI) controller. This is a feedback controller which commands the system with a weighted sum of the error and the integral of that value. The following derivations closely follow the work that

was done by Brennan in Ref. [2]. The actuator state integrator is given by

$$\mathbf{p}[k+1] = a\mathbf{p}[k] + \mathbf{u}[k], \tag{2.28}$$

where $\mathbf{p}[k]$ is the current command given to the DM and k is the discrete sample time. There is a damping factor a which is very close to one. Previous sensor measurements are used to build the control vector, $\mathbf{u}[k]$. The error, error estimate, and control law are defined by

$$\mathbf{e}[k] = \boldsymbol{\phi}[k] - \mathbf{p}[k] \tag{2.29}$$

$$\hat{\mathbf{e}}[k] = H\Gamma\mathbf{e}[k] \tag{2.30}$$

$$\mathbf{u}[k] = b_0\hat{\mathbf{e}}[k] + b_1\hat{\mathbf{e}}[k-1] + b_2\hat{\mathbf{e}}[k-2], \tag{2.31}$$

where b_0, b_1, and b_2 are constant control law parameters. The error $\mathbf{e}$ is the difference between the aberrated phase of the field and the phase imparted by the DM. The error estimate $\hat{\mathbf{e}}$ is the result of sensing the gradient of the error which is expressed by Γ and reconstructing the error with H. The control gains are applied to the sequence of error estimates to produce the actuator command vector [2]. Using the notation

$$B_j = b_j H\Gamma \tag{2.32}$$

and substituting Eqs. (2.29) to (2.31) into Eq. (2.28) results in the closed-loop equation

$$
\begin{aligned}
\mathbf{p}[k+1] \;=\; & a\mathbf{p}[k] + B_0(\boldsymbol{\phi}[k] - \mathbf{p}[k]) + \\
& B_1(\boldsymbol{\phi}[k-1] - \mathbf{p}[k-1]) + \\
& B_2(\boldsymbol{\phi}[k-2] - \mathbf{p}[k-2]).
\end{aligned} \tag{2.33}
$$

There are three cases for the general control law given in Eq. (2.31) for this research:

$$
\begin{aligned}
\text{Case 1} \quad &: \quad b_1 = b_2 = 0; \quad b = b_0 \\
\text{Case 2} \quad &: \quad b_0 = b_2 = 0; \quad b = b_1 \\
\text{Case 3} \quad &: \quad b_2 = 0; \quad b_0 = b_1 = 0.5b
\end{aligned}
\tag{2.34}
$$

Case 1 is a simple type 1 integrator, and is used for most of the studies in this research. Case 2 adds one degree of latency to the integrator, and Case 3 is a gain applied to the mean of the previous two measurements.

When using the Kolmogorov turbulence model, the residual phase due to finite control bandwidth σ^2_{Temp} of an AO system can be estimated by the closed-loop 3-dB bandwidth of the system f_{3dB} and the Greenwood frequency: [7]

$$
\sigma^2_{Temp} = \left(\frac{f_G}{f_{3dB}} \right)^{5/3} .
\tag{2.35}
$$

The Greenwood frequency is an important part of the simulation. As the Greenwood frequency gets larger, the AO system lags behind the turbulence, and so the performance of the system degrades. In order to maintain performance, the sampling frequency or control gain must increase to maintain a constant relationship between Greenwood frequency and 3-dB bandwidth of the system. As a rule, AO systems should have a f_{3dB} of at least ten times larger than the Greenwood frequency. For Case 1, the 3-dB frequency is

$$
f_{3dB} = \frac{b f_s}{2\pi},
\tag{2.36}
$$

where f_s is the sampling frequency.

2.4 Misregistration

Misregistration refers to the uncertain knowledge of the relative optical alignment of the DM's actuators and the WFS's subapertures. Any amount of misregistra-

tion will cause a degradation in the performance of an AO system. There are different types of misregistration, including optical, rotational, and translational misregistration. Optical misregistration is usually dealt with during the setup of the optical system. Careful design and production can remove optical misregistration. The main focus of this research is translational misregistration, which creeps into all optical systems and is very difficult to remove completely. Because of this difficulty, different mitigation strategies have been developed to compensate for translational misregistration. In order to understand misregistration, it is important to understand the mathematical models of AO measurements. The slope measurements produced in a subaperture by pushing a single DM actuator are a basis for forming the linear model relating actuator commands to sensor measurements. This section is based on the research and technical reports completed by Brennan [2, 3].

The basis of this research is that the subapertures are square, and the subaperture sensor measures the average gradient of the phase over the sensing region. The actuators are aligned on the corners of the subaperture (Fried geometry, as discussed in Sec. 2.3.1.1). Translational misregistration is the lateral shift from the nominal position as shown in Fig. 2.11. The slopes within a subaperture are measured in two directions, $\mathbf{s} = (s_x, s_y)$. These are average phase differences over the subaperture area, given by

$$
\begin{aligned}
s_x &= \int_0^1 dy(\phi(1, y) - \phi(0, y)), \\
s_y &= \int_0^1 dx(\phi(x, 1) - \phi(x, 0)),
\end{aligned}
\tag{2.37}
$$

where $\phi(x, y)$ is the phase to be measured. For Eq. (2.38) the units of x and y will be taken to be in actuator spacing so that the distance between an actuator and its nearest neighbor is unity. The actuator influence function $\mathcal{A}_{kl}$, is the phase caused by poking an individual actuator. It is assumed that $\mathcal{A}_{kl} = 1$ at the location (k, l). The
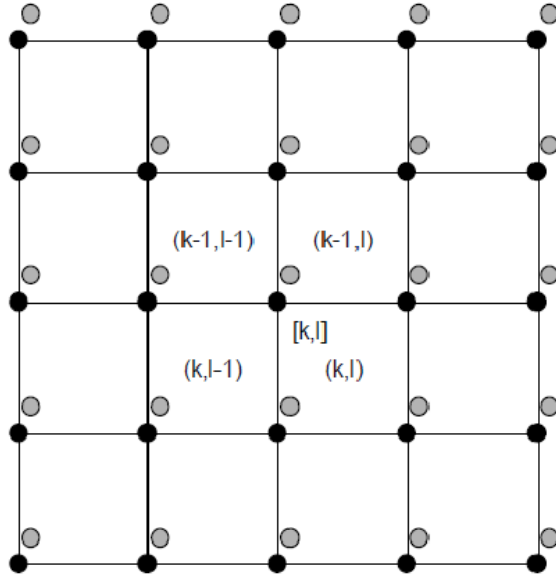
Figure 2.11:   The squares represent the SH WFS subapertures.
The dark spots represent nominal actuator positions, and the
gray spots are actuators misregistered with respect to the sub-
apertures. The ordered pairs illustrate the indexing convention
in this section's equations. The square bracket indicates actua-
tor indices, and the round brackets are subaperture indices.

influence function is given by

$$
\mathcal{A}(x, y) = \begin{cases} 0 & , \quad \text{if } |x| > 1 \text{ or } |y| > 1, \\ 1 - |x| & , \quad \text{if } |y| \leq |x|, \\ 1 - |y| & , \quad \text{if } |x| \leq |y|. \end{cases} \tag{2.38}
$$

For the actuator (k, l) the influence function is $\mathcal{A}_{kl}(x, y) = \mathcal{A}(x - k, y - l)$. With misregistration of (δ_x, δ_y) at actuator (k, l), the (m, n)-subaperture measures

$$
\tilde{s}_x = \int_0^1 dy [\mathcal{A}_{kl}(n - l + 1 - \delta_x, m - k + y - \delta_y) - \mathcal{A}_{kl}(n - l - \delta_x, m - k + y - \delta y)],
$$
$$
\tag{2.39}
$$
$$
\tilde{s}_y = \int_0^1 dx [\mathcal{A}_{kl}(n - l + x - \delta_x, m - k + 1 - \delta_y) - \mathcal{A}_{kl}(n - l + x - \delta_x, m - k - \delta y)].
$$

With proper registration, the result of poking a single actuator is to produce signals in the four subapertures adjoining the actuator. However, with misregistration that number can increase to nine different subapertures.

Misregistration increases the system's sensitivity to loss of phase margin, thereby decreasing its stability. However, other factors need to be examined to see the impact on phase margin. The system's stability depends on the servo law, the system size, and whether the edge actuators have a ring of slave actuators connected to them [2]. Larger systems tend to be more sensitive to misregistration instability. Stability sensitivity is a question of how the eigenvalues of a matrix are perturbed by changes in system parameters [2]. This means that small changes in many entries of a large matrix can have great effect on the eigenvalues of $H\Gamma$. This is the exact effect of misregistration. Larger systems have more actuators and subapertures, and therefore are more sensitive to misregistration than smaller systems. Moreover, misregistration is measured as a fraction of a subaperture, so when considering the actual physical displacement, the size of the system is more significant. For example, suppose a 10×10 AO system in a 1 meter aperture can tolerate 10% of a subaperture while a 20×20

can only tolerate 5%, a factor of 2 less. The 10×10 system can actually tolerate 1 cm of shift while the 20×20 can only tolerate 2.5 mm, a factor of 4 less [2].

The SH WFS, which has been the traditional WFS for AO, has multiple mitigation strategies to deal with misregistration. However, due to the new development of the SRI WFS, no mitigation strategies have been developed for an AO system using this type of WFS. This research outlines a mitigation strategy that decreases the need for such precise and time-consuming hand alignment of the AO system. This research shows that SRI WFS performance can be maintained with surprisingly large misregistration in the system.

The use of spatial filtering techniques has been shown to reduce the stability margin loss in the SH WFS. The spatial filtering method uses the principles of Fourier optics to alter the structure of a field. It has many uses, including removing the high-frequency modes. Modes correspond to the individual eigenvalues and have distinctive phase profiles that can be seen on the DM surface. The modes that exhibit significant high-frequency content appear as local waffle on the DM, seen in Fig. 2.12. The mechanism for instability is the loss of phase margin in high-frequency modes. This suggests the idea that attenuating the high-frequency spatial response would reduce the stability sensitivity to misregistration [3]. Two specific two-dimensional spatial convolution filters have been developed, the T-filter

$$T = \frac{1}{2} \begin{bmatrix} 0 & \frac{1}{4} & 0 \\ \frac{1}{4} & 1 & \frac{1}{4} \\ 0 & \frac{1}{4} & 0 \end{bmatrix}, \tag{2.40}$$

and the W-filter

$$W = \frac{1}{4} \begin{bmatrix} \frac{1}{4} & \frac{1}{2} & \frac{1}{4} \\ \frac{1}{2} & 1 & \frac{1}{2} \\ \frac{1}{4} & \frac{1}{2} & \frac{1}{4} \end{bmatrix}. \tag{2.41}$$
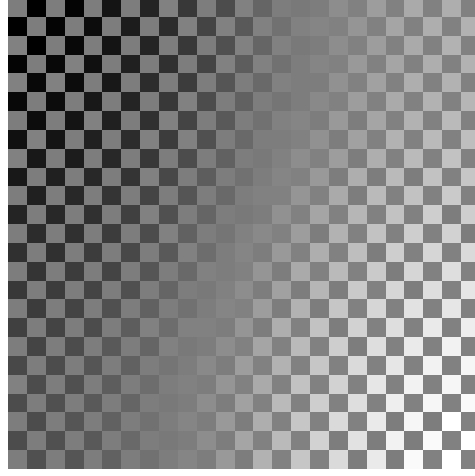
Figure 2.12: Local waffle pattern in mode indicates a potentially unstable mode of the system.

When these filters are convolved with local checkerboard patterns

$$
\begin{bmatrix} 0 & 1 & 0 \\ 1 & 0 & 1 \\ 0 & 1 & 0 \end{bmatrix} \quad \text{or} \quad \begin{bmatrix} 1 & 0 & 1 \\ 0 & 1 & 0 \\ 1 & 0 & 1 \end{bmatrix} \tag{2.42}
$$

the result is a constant $1/2$. These filters are applied by using a convolution with the reconstructed phase. For example, the equation for the W-filter can be written

$$
W \otimes \mathbf{a} = W \otimes H\mathbf{s}, \tag{2.43}
$$

where $\otimes$ represents convolution. The standard least-squares reconstructor's phase margin is compared to the T- and W-filter reconstructor phase margin in Fig. 2.13, for one and two frames of latency [3].

A more general spatial filter, called an actuator-penalty filter, has been developed by Gavel [5]. To penalize waffle, a positive-definite matrix is used as a actuator
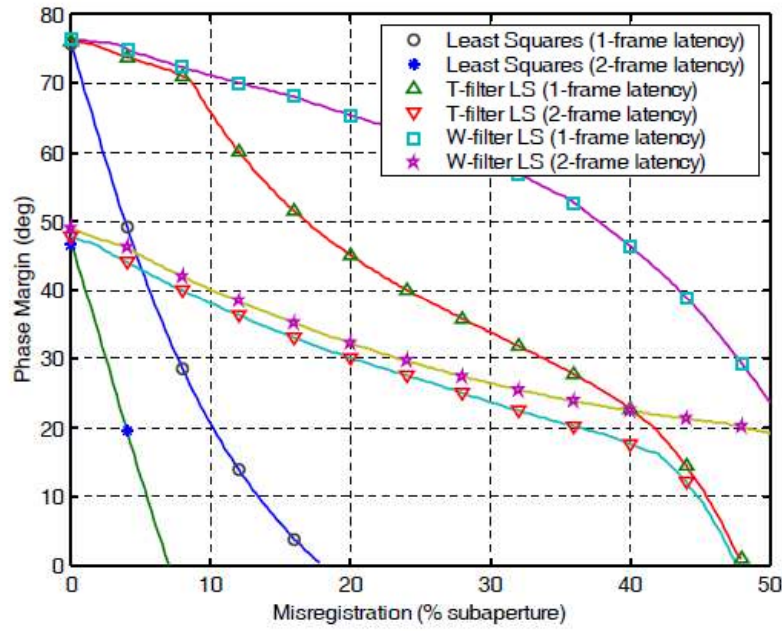
31

Figure 2.13: Phase margins were calculated for misregistration up to half of a subaperture and for servo latency of 1 and 2 frames. The least-squares reconstructor was evaluated as well as the least-squares followed by the T- and W-filters. Image courtesy of Ref. [3].

32

weighing. In order to penalize all local waffle behavior the weighting matrix

$$\mathbf{V} = F^T F \ , \tag{2.44}$$

where F is

$$F = \begin{bmatrix} 1 & -1 \\ -1 & 1 \end{bmatrix} \otimes \tag{2.45}$$

is the filter [5]. $\mathbf{V}$ is a rank N matrix that penalizes all localized waffle behavior, in that it actually changes the mode space structure. This arises by defining a waffle-penalized metric similar to the least-squares. This metric is given by

$$J = (\mathbf{s} - H\mathbf{a})^T (\mathbf{s} - H\mathbf{a}) + \mathbf{a}^T \mathbf{V} \mathbf{a}. \tag{2.46}$$

The result of the least-squares, waffle penalized and T-filter reconstruction modes are shown in Fig. 2.14. The least-squares modes clearly show local waffle in each mode, while modes from the other two techniques are free of local waffle. A full mathematical explanation of the development of actuator penalty can be found in Ref. [5].

While these techniques work by increasing the phase margin on a misregistered AO system, a few problems still remain. First, these strategies use an unrealistic influence function. They assume a pyramidal influence function on a continuous DM, while the true influence function is typically Gaussian [10]. Also, these strategies do not account for misregistration; they simply have less sensitivity to it. The development of a poke matrix as a mitigation strategy will address both of these issues.

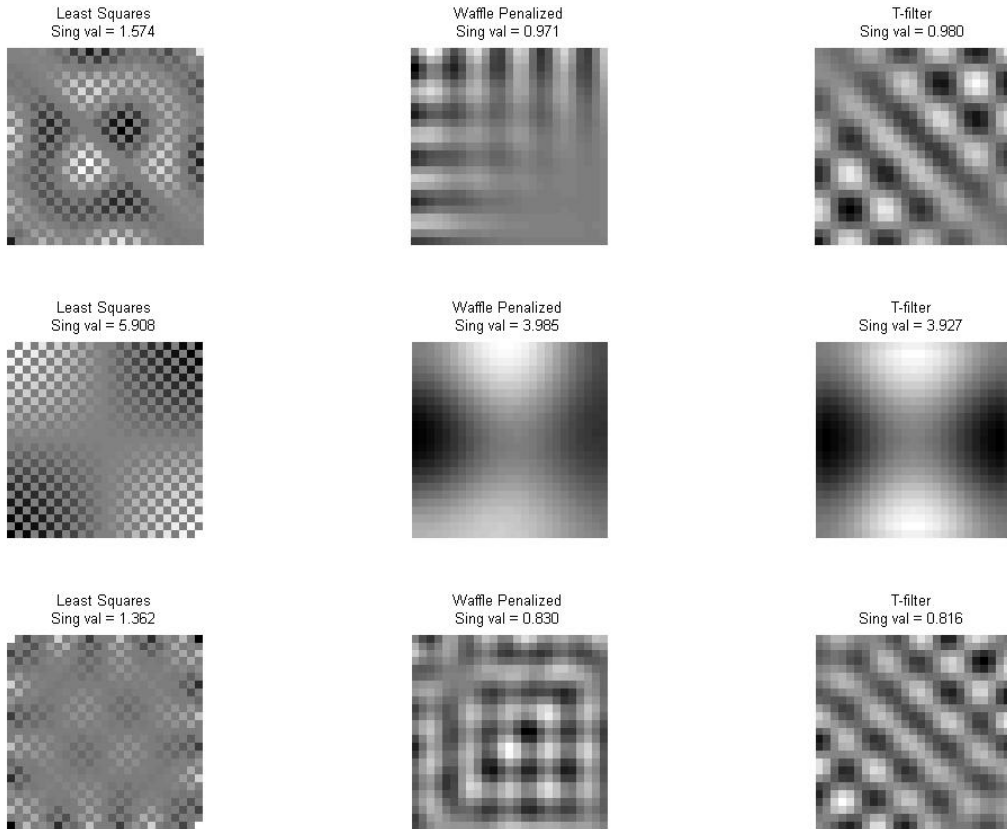Figure 2.14: An assortment of 3 modes shows the local waffle in the least-squares reconstructor. Both the waffle-penalized reconstructor and the T-filter reconstructor remove the local waffle. Local waffle increases the instability of the system.

III. Methodology

This chapter develops the methods used to conduct this research. In order to perform these studies, an AO system was modeled and then different techniques were used to find the geometry matrix. First, the chapter introduces the software used throughout the research. Next, it explains the poke geometry matrix and describes the analytical calculations for stability. Three criteria were used to examine the stability of each system: first, an examination of the poles of the closed-loop transfer function, second, the effects an exploration of gain combined with misregistration, and third, an evaluation of the phase margins of the system. After calculating the stability for each system, simulations were conducted to show how each matrix performs. All simulations used for this research were conducted in `Matlab`® software, specifically with the WaveProp toolbox provided by the Optical Sciences Company [4]. The studies explored how misregistration affected the SH WFS and SRI WFS.

3.1   *WaveProp*

The wave optics simulation system, WaveProp, is a toolbox for `Matlab`® . Based on object oriented programming (OOP), it provides a powerful tool for numerical simulations of wave propagation through turbulence and operation of AO components. WaveProp provides over 65 different objects that the user can leverage to build up simulations of laser engagements and AO system operation. This allows users to easily develop their own specialized models. These different objects range from simple electromagnetic fields to complex optical devices such as WFSs and DMs. In the modeling of wave optics propagation, electromagnetic fields are generally represented as two-dimensional arrays of complex numbers [4]. WaveProp packages these arrays with units and physical dimensions to facilitate use of the arrays.

3.2   *Geometry matrix*

AO system designers need to determine the relationship between the WFS measurements and the actuator commands on the DM. A geometry matrix Γ is used to

map this relationship, as discussed in Chapter 2. The model Γ discussed in Chapter 2 assumes a perfect optical alignment between the DM actuators and WFS subapertures. Most AO systems have approximately the same number of actuators and subapertures, so Γ has approximately $2n$ rows (2 slopes per actuators) and n columns where n is the number of actuators. The first part of this research is building this geometry matrix with and without misregistration on the system. Two ways to build Γ have been used in this study: single-actuator poke and multiple-actuator poke.

3.2.1 Single Actuator. The single-actuator poke is the simplest of ways to build Γ through measurements. It is a basic method of poking a single actuator on the DM and recording the slopes measured by the WFS. As mentioned in Section 2.3, the WFS measurements comprise x and y components of the wavefront gradient. The DM's actuators are numbered in a column-major order starting with the upper left hand corner as shown in Fig. 2.5.

Because the WFS measures the local slopes, the magnitude of the poke on the DM's actuator must be taken into consideration. Each actuator must be poked at the same magnitude, and then the slopes need to be normalized by the magnitude of the poke.

A simple example of this procedure appears in Fig. 2.5. The columns of Γ are equated to the numbered position of the DM's actuators. The top half of the rows in Γ represent the measured x slopes, while the bottom rows represent the y slopes. To build Γ, the first step is to poke actuator 1 of the DM, which gives a maximum x slope WFS measurement at position (1,1) of the matrix. A maximum y slope measurement is also recorded in position (17,1), with this being the first row that represents y slopes. To finish building the matrix, each actuator is poked, and the measured slopes are recorded.

In this example there are a total of 25 actuators on the DM. For this small number of actuators, the single-poke method can build the geometry matrix fairly quickly. However, with larger DMs the number of actuators rapidly increases, and the single-actuator method becomes time consuming. A faster method is necessary to maintain efficiency.

3.2.2 Multiple Actuators.   In order to increase the speed of building Γ, it is possible to push multiple actuators at the same time. However, simultaneously pushing multiple actuators means a few added details need to be addressed. The procedure for setting up multiple pokes is important; this study used a checkerboard pattern. Additionally, it is necessary to identify which measured slope goes with which actuator. The output of the WFS is arranged into a vector. The first half of the vector gives the x slopes, and the second half of the vector gives the y slopes. When using more than one actuator, the output vector needs to be broken into sections that are assigned to specific columns of the geometry matrix. After each section is placed into the correct column, the other positions in the column are set to zero. Each column of the geometry matrix represents the number position of the actuator on the DM.

For example, again looking at the DM in Fig. 2.5, assume that actuators 1 and 21, the top corner actuators, were pushed at the same time. The output vector of the WFS would indicate slope measurements in rows 1 and 17 for actuator 1. However, there would be an additional measurement in rows 13 and 29 for actuator 21. To build Γ, the measurements of the slopes in subapertures 1 and 17 would need to go into the first column, while the measurements of the slopes in subapertures 13 and 29 would need to be placed into column 21.

This example ignores the fact that a continuous DM was used. In a continuous DM, when one actuator is poked it affects the surrounding subapertures and gives

more than just one WFS measurement. This effect is known as the influence function of the DM.

3.2.2.1 *Influence Function.* The influence function is how much the movement of one actuator affects the position of its neighboring actuators. For a registered system, the effect of one actuator is normally limited to the four neighboring actuators. For a misregistered system, there is not a simple alignment of maximum slopes with the pushed actuators. This increases the number of subapertures affected by a single actuator to as many as nine. The actuator influence function requires that, when building a geometry matrix through poking multiple actuators, the actuators are far enough apart to ensure that they do not influence each other. Recall that a more complete analysis of the actuator influence function is covered in Sect. 2.4. For the 16×16 actuator DM, the multiple-actuator method was used. The separation of the pokes between actuators was set to five subapertures. Using the multiple-actuator method in the 16×16 subaperture system reduced the number of data sets from 289 to less than 40 to build the Γ matrix.

3.2.3 *Phase Reconstructor.* Once Γ has been built, the final step is to use Γ to calculate the phase reconstructor matrix H. As discussed in Chapter II, a least-squares pseudo-inverse method is used. This usually provides a reasonably accurate answer, however Γ may be rank deficient. The Fried geometry has two null modes, which are two orthogonal types of waffle, so the rank deficiency of Γ is 2. Some solutions for the AO system are not explicitly defined via the least-squares pseudo-inverse [5].

A more rigorous method of computing H is to use singular value decomposition (SVD). The SVD method finds the solution of minimum norm and can give a solution that has no projection into the null space. The Γ matrix can be written as the product

$$\Gamma = B\Sigma A^T .$$
(3.1)

If n_a is the number of actuators, A is an $n_a \times n_a$ matrix with orthonormal columns and rows (that is, $A^T = A^{-1}$), B is and $n_s \times n_a$ matrix with orthonormal columns ($B^T B = I$), and $\Sigma = \text{diag}(\sigma_i)$ is a diagonal matrix with nonnegative diagonal elements σ_i [5]. The modes of the actuator space are defined by the columns of A, and the normalized sensor responses are defined in the columns of B. The mode measurability, or the strength of the sensor's response to actuator mode i is the quantity σ_i. When $\sigma_i = 0$, the corresponding mode is in the null space of Γ. The null modes can be removed as described below.

The functors A and B can be written as $A = [a_1|a_2|\dots|a_{na}]$ and $B = [b_1|b_2|\dots|b_{na}]$. This interpretation gives the ability to remove columns of A and B that contain null modes. Say that the rank of Γ is r. Let A' be a matrix that contains only the first r columns of A, let B' be a matrix that contains only the first r columns of B, and let Σ' be a matrix of appropriate size with the nonzero σ_i values on its diagonal. Then the modified reconstructor is

$$H = B'\Sigma' A'^T, \tag{3.2}$$

where $B'^T B' = I$ and $A'^T A' = I$, so $H^T H = A' \Sigma'^2 A'^T$. A comparison was made of the SVD reconstruction matrix with the least-squares reconstruction matrix; the performance of each was nearly identical.

3.3   Stability Verifications

Several tests were conducted to check AO system stability. These tests follow the methods developed in Ref. [2]. The stability tests of the system used the closed-loop poles of the transfer function. In order to find the transfer function, the state space equations needed to be computed. The first-order state space equations for the

AO system defined by Eq. (2.34) can be written as

$$
\begin{pmatrix} \mathbf{p}[k+1] \\ \mathbf{p}[k] \\ \mathbf{p}[k-1] \end{pmatrix} = \begin{pmatrix} aI - B_0 & -B_1 & -B_2 \\ I & 0 & 0 \\ 0 & I & 0 \end{pmatrix} \begin{pmatrix} \mathbf{p}[k] \\ \mathbf{p}[k-1] \\ \mathbf{p}[k-2] \end{pmatrix} + \quad (3.3)
$$
$$
\begin{pmatrix} B_0 & B_1 & B_2 \\ 0 & 0 & 0 \\ 0 & 0 & 0 \end{pmatrix} \begin{pmatrix} \phi[k] \\ \phi[k-1] \\ \phi[k-2] \end{pmatrix},
$$

where I and 0 are the identity and zero matrices of the appropriate size. The stability of Eq. (3.4) is due to the eigenvalue locations of the closed-loop matrix

$$
A = \begin{pmatrix} aI - B_0 & -B_1 & -B_2 \\ I & 0 & 0 \\ 0 & I & 0 \end{pmatrix}. \quad (3.4)
$$

To state that the system is stable, all the eigenvalues of A need to lie within the unit circle of the complex plane. It can be stated that the stability condition for Eq. (3.4) is

$$
|\mu| < 1, \quad \text{for all } \mu \in \Lambda(A), \quad (3.5)
$$

where the operator $\Lambda(\cdot)$ indicates the eigenvalues of a matrix.

Finding the numerical eigenvalues of A can be extremely time consuming due to the size of the matrix A. It has been shown that $\Lambda(A)$ can be obtained as the solution of polynomial equations with coefficients which are a function of $\Lambda(B_j)$. From the definition of B_j in Eq. (2.32) it is clear that [2]

$$
\Lambda(B_j) = b_j \Lambda(H\Gamma). \quad (3.6)
$$

For many values of the gain b_j, it is possible to solve the smaller eigenvalue problem, $\Lambda(H\Gamma)$ once instead of the larger problem of the eigenvalues of A. Using the definition of an eigenvalue and substitution into Eq. (2.32) leads to

$$\mu^3 - (aI - b_0 H\Gamma)\mu^2 + b_1 H\Gamma\mu + b_2 H\Gamma = 0, \qquad (3.7)$$

where the solutions μ are the eigenvalues of A. It is assumed that $H\Gamma$ has a diagonal eigenvalue decomposition,

$$H\Gamma = DED^{-1} \qquad (3.8)$$

where the eigenvalues of $H\Gamma$ are on the diagonal of the diagonal matrix E. With this assumption Eq. (3.7) can be diagonalized with D. Multiplying the matrix D to the right side of Eq. (3.7) and D^{-1} to the left side gives

$$\mu^3 - (aI - b_0 E)\mu^2 + b_1 E\mu + b_2 E = 0. \qquad (3.9)$$

If there are n eigenvalues in $\Lambda(H\Gamma)$, this equation gives n simple independent equations. Now, for a given set of gains a, b_0, b_1, and b_2, the closed-loop system is stable if and only if for each $\lambda \in \Lambda(H\Gamma)$ the three solutions of

$$\mu^3 - (aI - b_0\lambda)\mu^2 + b_1\lambda\mu + b_2\lambda = 0 \qquad (3.10)$$

all have magnitudes less than unity [2]. This can be called the characteristic equation for stability.

Now looking at the three cases shown by Eq. (2.34), the three characteristic equations are

$$\begin{aligned} \text{Case 1} \quad &: \quad \mu - (a - b\lambda) = 0 \\ \text{Case 2} \quad &: \quad \mu^2 - a\mu + b\lambda = 0 \\ \text{Case 3} \quad &: \quad \mu^2 - (a - 0.5b\lambda)\mu + 0.5b\lambda = 0 \ . \end{aligned} \qquad (3.11)$$

When the solutions of $\mu = 0$ have been factor out, these solutions can be simplified to

$$
\begin{aligned}
\text{Case 1} \quad &: \quad \mu = a - b\lambda, \\
\text{Case 2} \quad &: \quad \mu = 0.5(a \pm \sqrt{a^2 - 4b\lambda}), \\
\text{Case 3} \quad &: \quad \mu = 0.5[a - 0.5b\lambda \pm \sqrt{(a - 0.5b\lambda)^2 - 2b\lambda}].
\end{aligned}
\tag{3.12}
$$

For the ideal case where the reconstructor H is the exact pseudo-inverse of Γ, the $\Lambda(H\Gamma)$ are all unity except for the unobservable actuator modes which are zero. For this research the measured matrix $\hat{\Gamma}$, which is the true mapping of actuators to sensors, was used instead of the ideal Γ matrix.

Three tests were used to determine the stability of the AO system. First, the closed-loop poles of the transfer function were examined. Second, a contour plot was developed showing what effects gain coupled with misregistration have on the system. Third, the phase margins of the open-loop transfer function were calculated.

3.3.1 Transfer Function Poles. As described above, the first test of stability is to examine the poles of the transfer function of the closed-looped system. Each eigenvalue of $\Lambda(H\Gamma)$ is used in Eq. (3.12) to determining the closed-loop poles of the system. With the model matrix and no misregistration, all the eigenvalues are either zero or one. As the system is misregistered, the eigenvalues change and therefore the poles approach the unit circle, corresponding to instability. WaveProp is able to model the geometry matrix $\hat{\Gamma}$ when a known amount of misregistration is placed on the system. With $\hat{\Gamma}$ and using the the reconstructor H, the closed-loop poles of the system are found and shown in Fig. 3.1.

The measured poke matrix is used to show greater stability of the reconstructor by examining the transfer function closed-loop poles. Two different reconstruction matrices were found, one corresponding to the SH WFS and the other corresponding to the SRI WFS. Viewing these two sets of plots helps to determine which system is
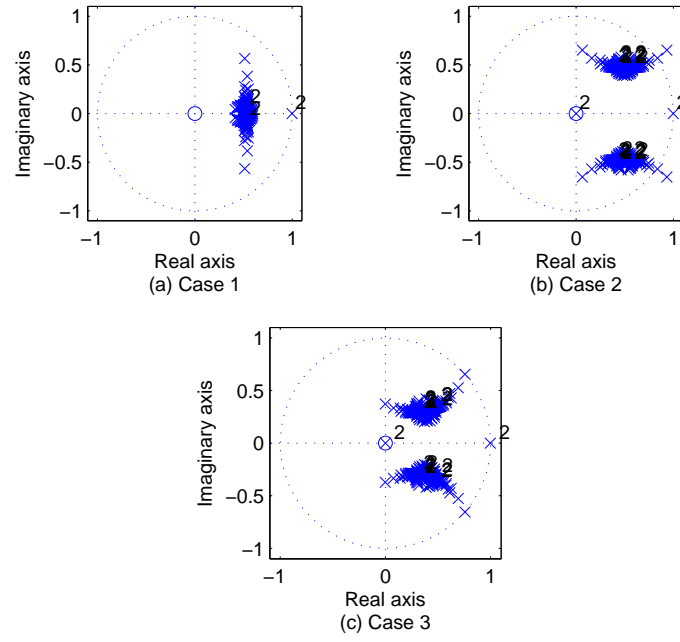
Figure 3.1: Closed-loop pole locations are plotted for a misregistration of $\delta = 0.12$ subapertures. The three cases are defined in Eq. (2.34) with solutions in Eq. (3.12). This is 15×15 subapertures with servo gains of $a = 0.998$ and $b = 0.5$.

more stable. The poles of the system are not only affected by the eigenvalues of $H\Gamma$ but also by the the gain b.

3.3.2 Gain and Misregistration. The effects of coupling gain and misregistration are shown, and their relationship to each other and instability determined. For the simple integrator, Case 1 described by Eq. (2.34), the varying of b has been shown to affect the stability of the system. Looking at the closed-loop poles as defined for Case 1 in Eq. (3.12), the relationship of servo gain and misregistration can be shown. The set of closed-loop poles for this system are [2]

$$a - b\Lambda(H\Gamma(\delta,\delta)) = \{a - b\lambda : \lambda \in \Lambda(H\Gamma(\delta,\delta))\}. \qquad (3.13)$$

The magnitude of the largest closed-loop pole of a misregistered system with a set δ, a, and b is shown as

$$\mathcal{M}(\delta,a,b) = \max(|a - b\Lambda(H\Gamma(\delta,\delta))|). \qquad (3.14)$$

Using this equation, the unity contour line of the system can be found. The contour line shows which combinations of gain and misregistration can be on the system without affecting stability. This plot is shown later in Fig. 4.2.

The contour line of the SH system was calculated for both the WaveProp-generated $\hat{\Gamma}$ and the measured $\hat{\Gamma}$. In order to build the contour line, the system was misregistered between 0% to 50% of a subaperture. There were 20 misregistration steps in the plot. At each misregistration step, there were 50 steps of gain between 0 to 1. Then Eq. (3.14) was used to find the unity contour line. Later in Fig. 4.7 the stability line for the SRI is compared to both stability lines of the SH. The next stability calculation involved the phase margins of the system, as well as other mitigation phase margins.

3.3.3 Stability Margins.   Before instability is reached, the system's performance and stability margins may decrease. This decrease is tracked by examining the phase margins of the system. The open-loop transfer function is used to discover how misregistration affects the stability margins. The open-loop transfer function is found by combining Eqs. (2.28), (2.30) and (2.31) to give

$$\mathbf{p}[k+1] = a\mathbf{p}[k] + b_0 H\Gamma\mathbf{e}[k] + b_1 H\Gamma\mathbf{e}[k-1] + b_2 H\Gamma\mathbf{e}[k-2]. \qquad (3.15)$$

Again diagonalizing the equation as shown above yields

$$\begin{aligned} q_\lambda[k+1] &= aq_\lambda[k] + b_0\lambda f_\lambda[k] + b_1\lambda f_\lambda[k-1] + b_2\lambda f_\lambda[k-2] \\ &= aq_\lambda[k] + \lambda(b_0 f_\lambda[k] + b_1 f_\lambda[k-1] + b_2 f_\lambda[k-2]), \qquad (3.16) \end{aligned}$$

where

$$\mathbf{q} = D^{-1}\mathbf{p} \qquad (3.17)$$

$$\mathbf{f} = D^{-1}\mathbf{e} . \qquad (3.18)$$

Because the equation has been diagonalized, Eq. (3.16) is a system of n independent single-input, single-output equations, one for each eigenvalue of $H\Gamma$. Equation (3.16) has been simplified using $\mathbf{q} = [q_\lambda]$ with λ being the eigenvalues of the matrix $H\Gamma$. For Case 1 in Eq.(2.34), Eq. (3.16) can be simplified to

$$q_\lambda[k+1] = aq_\lambda[k] + b\lambda f_\lambda[k-n]. \qquad (3.19)$$

For each of the n equations, the transfer function in the z-domain is analyzed to get the gain and phase margin. The transfer function in the z-domain of Eq. (3.19) is [3]

$$T_\lambda(z^{-1}) = \lambda\frac{bz^{-n}}{1 - az^{-1}} . \qquad (3.20)$$

45

The gain and phase margins for the system are the minimum gain and phase margins of the eigenvalues. If $g_m(\lambda)$ and $p_m(\lambda)$ are the gain and phase margins for the mode corresponding to eigenvalue λ, the the system gain and phase margins are defined by [2]

$$G_M = \min\{g_m(\lambda) : \lambda \in \Lambda(H\Gamma)\}$$
$$P_M = \min\{p_m(\lambda) : \lambda \in \Lambda(H\Gamma)\} . \tag{3.21}$$

With the analytical calculations completed the next step was to build simulations to see how misregistration affects the performance of the AO system.

3.4   Simulations

In order to understand misregistration better, a set of simulations was performed, and the measured Strehl ratios were used to judge AO system performance. These simulations explored several different aspects of the performance of the system in the presence of misregistration. Each simulation was set up as shown in the diagram in Fig. 2.3. The simulations were composed of five major components: the object source, the phase screen, the DM, the imaging camera, and the WFS.

The object source was modeled as a point source, with a wavelength of 1 μm. The point source was assumed to be very far away so that the incoming field could be modeled as a plane wave, an electromagnetic field represented on a grid with 256×256 samples over the field. The source field was passed through a phase screen, thereby adding the distortion due to the atmosphere. The phase screen has specific characteristics to indicate how much phase distortion is added and how quickly the screen is moving. The strength of the distortion is indicated by the Fried parameter $r_0 = 37.5$cm. This value of r_0 was chosen in order to have the ratio of $d/r_0 = 0.5$, where d is the diameter of one subaperture of the WFS. The d/r_0 ratio is important in

that it indicates how much fitting error the system has on it, as discussed in Chapter II.

The phase screen also has a sampling of 256×256 and laterally translates at different velocities for each simulation. The velocity at which the phase screen moves is directly related to the Greenwood frequency of the turbulence according to Eq. (2.12). The metric used to calculate the velocity of the phase screen was a ratio of the 3-dB bandwidth of the system over Greenwood frequency. For each set-up, the simulation ran with $f_{3dB}/f_G = 2,\ 5,\ 10,\ 15$.

After the field passed through the phase screen, it was reflected off the DM. The DM was set up to minimize the residual error sensed by the WFS. Each DM used in the simulations was set up to be a square mirror without any actuator slaving. These DMs were continuous facesheet DMs and had two different sets of resolution. The small DM, with 64 actuators arranged in an 8×8 square, was tested to see how coarser resolution DMs perform with misregistration. It was predicted that the small DM would be able to handle the misregistration better, but that its overall performance would be less successful. The other DM, with 256 actuators arranged in a 16×16 square, was tested to see how finer resolution DMs perform with misregistration. The finer resolution of this mirror should have a greater overall performance, but misregistration should cause it to lose stability more quickly. Once the field was reflected off the DM, the Strehl ratio was calculated. The field estimated Strehl ratio used in these simulations is given by

$$SR = \frac{|\sum U|^2}{\sum |U|^2},\tag{3.22}$$

where U is the compensated optical field. The field was then measured by the WFS and commands were given to the DM for the next time step. This process used the control law developed in Sec. 2.3.3. The 16 simulation cases are enumerated in Table
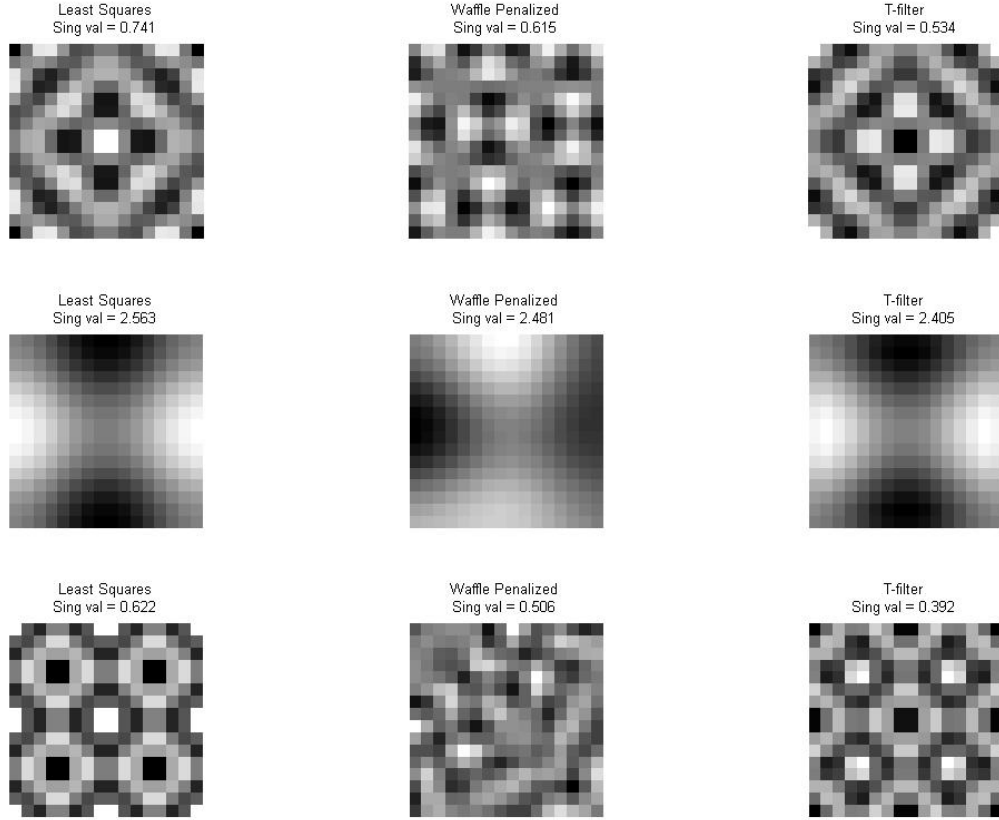
47

Least Squares
Sing val = 0.741

Waffle Penalized
Sing val = 0.615

T-filter
Sing val = 0.534

Least Squares
Sing val = 2.563

Waffle Penalized
Sing val = 2.481

T-filter
Sing val = 2.405

Least Squares
Sing val = 0.622

Waffle Penalized
Sing val = 0.506

T-filter
Sing val = 0.392

Figure 3.2: An assortment of 3 modes shows the local waffle in the least-squares reconstructor. Both the waffle-penalized reconstructor and the T-filter reconstructor remove the local waffle. Local waffle increases the instability of the system.

3.1.

These simulations were conducted using the SH WFS and the SRI WFS separately. The SH WFS has a more fully developed model, and WaveProp has tools to compute a misregistered Γ matrix. As shown in Fig. 2.14, SH WFS modes are plagued by local waffle when the least-squares reconstructor is used. As discussed in Sec. 2.4, the local waffle pattern represents high frequency content, which leads to the instability of the system. For the SRI WFS, an assortment of these modes can be seen in Fig. 3.2. There is very little local waffle in these modes. This leads

Table 3.1:   Simulation Parameters

Case #	WFS	f_{3dB}/f_G	DM size
1	SH	2	8×8
2	SH	5	8×8
3	SH	10	8×8
4	SH	15	8×8
5	SH	2	16×16
6	SH	5	16×16
7	SH	10	16×16
8	SH	15	16×16
9	SRI	2	8×8
10	SRI	5	8×8
11	SRI	10	8×8
12	SRI	15	8×8
13	SRI	2	16×16
14	SRI	5	16×16
15	SRI	10	16×16
16	SRI	15	16×16

to the hypothesis that the SRI provides a more stable system and less sensitively to translational misregistration.

IV. Results and Analysis

This chapter provides results for the analytical calculations and performance results of the simulations developed in Chapter III. After completion of the analytical calculations, the simulations were set up, and the performance of the AO system in each simulation was scored using the Strehl ratio. The first section in this chapter describes the development of the reconstruction matrix using the SH WFS. These results are compared with the next section that used the SRI WFS to calculate the reconstruction matrix.

4.1 Shack-Hartmann Reconstruction Matrix

Analytical calculations were completed on a general setup for a SH WFS using the Fried geometry. Three analytical calculations were completed, and the stability of the system identified. Two simulations were set up using the SH WFS, an 8×8 subaperture system, and a 15×15 subaperture system. Different levels of misregistration and different f_{3dB}/f_G levels were tested on the systems.

4.1.1 Analytical Calculations. The first analytical calculations were for the SH reconstructor matrix. Figure 4.1 shows the closed-loop poles of the system which were plotted using Eq. (2.34) with the solutions in Eq. (3.12). They were based on the eigenvalues of the matrix product $H\hat{\Gamma}$, with $\hat{\Gamma}$ generated using the poke method. $\hat{\Gamma}$ was generated with a misregistration of $\delta = 0.12$ subapertures. The control gains were $a = 0.998$ and $b = 0.5$. This graph shows that in contrast with Fig. 3.1, this system has stability in Cases 2 and 3. This suggests that with the poke method, the system both handles latency better and remains stable.

The next test examines the coupling effects of gain and misregistration. In Fig. 4.2 contour lines have been drawn. The graph shows that when the combination of gain and misregistration are below the curve, the system is stable. This indicates that the built reconstruction matrix (the red curve) has a greater area of stability than
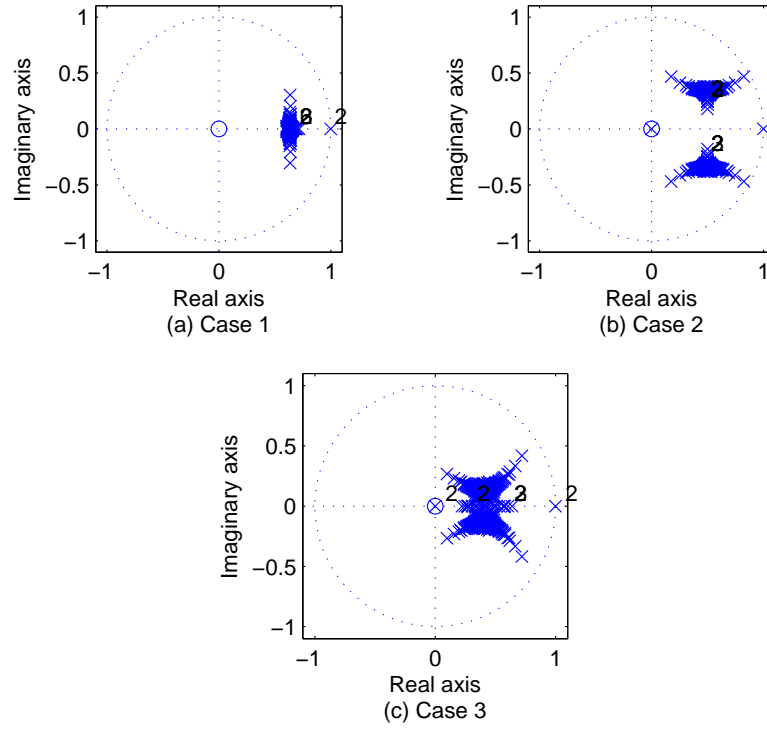
Figure 4.1: SH closed-loop poles for a 15×15 subapertures, the closed-loop poles are plotted for a misregistration of $\delta = 0.12$ subapertures. The three cases are defined in Eq. (2.34) with solutions in Eq.(3.12). The servo gains were $a = 0.998$ and $b = 0.5$. The Γ matrix was created using the poke method.
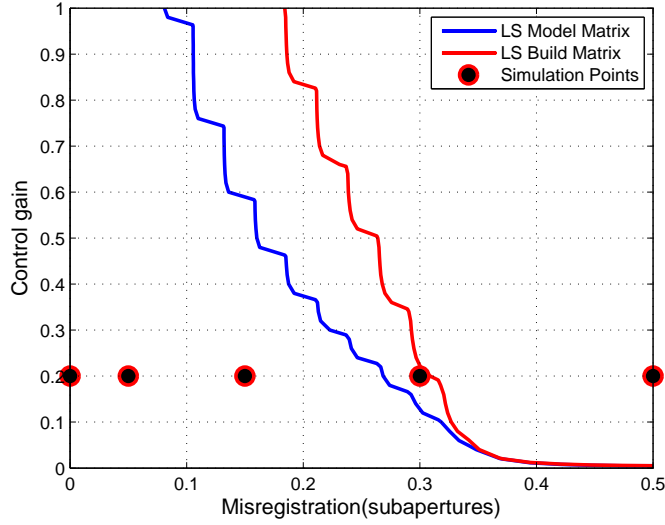
Figure 4.2:   Stability lines of a 15×15 subaperture system. This figure illustrates the relationship of instability with misregistration and gain. The area under the curves is the stable region, while the area above the curves is the unstable region. The least-squares model matrix refers to a WaveProp build reconstruction matrix, the least-squares build matrix refers to poke build SH reconstruction matrix. Both used the control law given in Eq. (3.12), Case 1.

the model matrix(the blue curve). The circles show the different misregistrations that were used in the simulations.

The final analytical result is displayed in Fig. 4.3. This graph shows that the measured reconstructor has better phase margins with misregistration than the model, but not as good as the T- and W-filters.

4.1.2   Simulation Performance.   Figure 4.4 gives the Strehl ratios of an 8×8 subaperture AO simulation. For plot (a), with $f_{3dB}/f_G = 5$ and misregistration of 5%, the simulations showed that for all reconstruction matrices the Strehl ratios were approximately equal. In fact, for all the different scenarios seen in the figure there is little variation among the Strehl ratios. This was due to the fact that the 8×8 subaperture system is a smaller system and is less affected by misregistration. The performance is poor as well, which might be due to the edge effects of a small
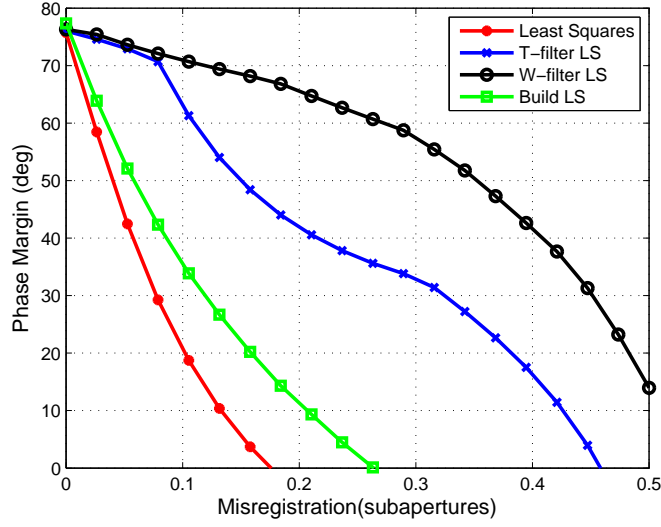
Figure 4.3: Phase margins of a 15×15 subaperture system. This figure illustrates the phase margins that were calculated for misregistration up to half of a subaperture. The model least-squares reconstructor was evaluated as well as the build least-squares reconstructor and the T- and W- filters.

system. As shown in Table 4.1, when there is no misregistration the system still did not have a much higher Strehl ratio. This was due to the low resolution of the DM. There is no real change in performance due to misregistration because of the greater stability of a smaller subaperture setup. In Fig. 4.5 the 15×15 subaperture system has a greater general perfromance, with Strehl ratios between 0.5 and 0.7 on average. The only Strehl ratios to fall out of the region are for the model matrix reconstructor in plots (b) and (d). These two graphs are of the systems with the greater misregistration on them. This result is not too surprising as these points do fall around the edge of the stability region found in the analytical calculations. This shows that as the number of subapertures increases, so do the system's performance capabilities. However, it is more sensitive to misregistration. Detailed results of the different simulations can be found in Tables 4.1 and 4.2. These tables outline how the average Strehl ratio performed for each scenario. The tables show that the system has its best performances with a higher number of subapertures and low misregistration.
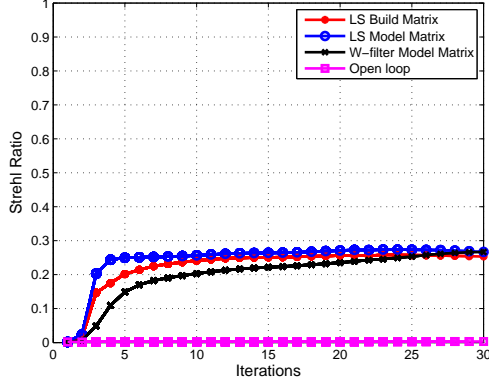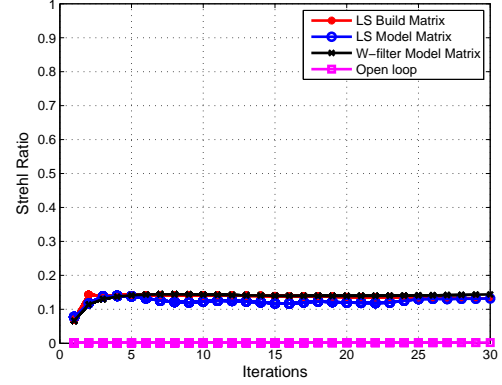
(a) Misregistration = 5%, $f_{3dB}/f_G = 5$
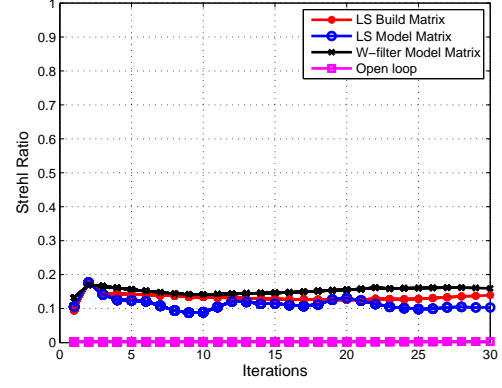
(b) Misregistration = 30%, $f_{3dB}/f_G = 5$
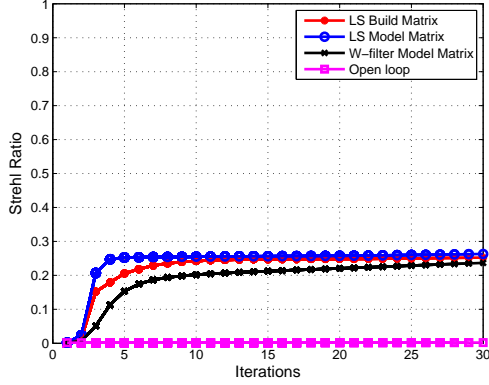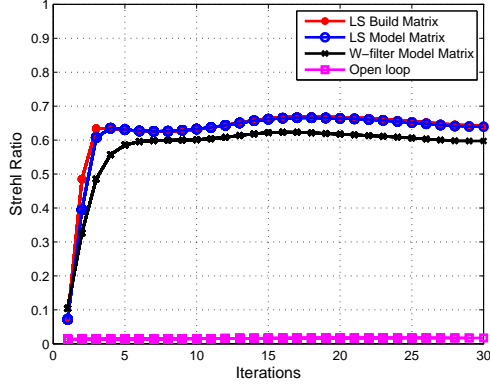
(c) Misregistration = 5%, $f_{3dB}/f_G = 15$

(d) Misregistration = 30%, $f_{3dB}/f_G = 15$

Figure 4.4:   This figure gives the results of a 8×8 subaperture AO system using a SH WFS run over 30 iterations. Four different reconstruction matrices are used to calculate the four Strehl ratios on each plot. The four reconstruction matrices are the least-squares build, the least-squares model, the W-filter and open-loop. (a) Shows the matrix having a misregistration of 5% of a subaperture with a $f_{3dB}/f_G = 5$. (b) Shows the matrix having a misregistration of 30% of a subaperture with a $f_{3dB}/f_G = 5$.(c) Shows the matrix having a misregistration of 5% of a subaperture with a $f_{3dB}/f_G = 15$.(d) Shows the matrix having a misregistration of 30% of a subaperture with a $f_{3dB}/f_G = 15$.

Table 4.1:   SH WFS Strehl ratio averages for a 8×8 subaperture system

| f_{3dB}/f_G	Misregistration %	Build Matrix Strehl Ratio	Model Matrix Strehl Ratio	% Change
2	0%	0.28	0.28	-1.3%
	5%	0.26	0.26	-2.2%
	15%	0.22	0.28	-0.6%
	30%	0.16	0.12	34.3%
	50%	0.02	0.0009	2311.1%
5	0%	0.27	0.28	-1.4%
	5%	0.25	0.27	-4.7%
	15%	0.21	0.23	-8.0%
	30%	0.13	0.11	21.8%
	50%	0.04	0.001	3354.5%
10	0%	0.26	0.27	-1.33%
	5%	0.25	0.26	-3.9%
	15%	0.21	0.23	-7.1%
	30%	0.14	0.13	6.5%
	50%	0.03	0.003	1016.1%
15	0%	0.26	0.27	-1.4%
	5%	0.25	0.26	-3.37%
	15%	0.21	0.22	-5.3%
	30%	0.14	0.13	8.4%
	50%	0.03	0.002	1230%

(a) Misregistration $= 5\%$, $f_{3dB}/f_G = 5$
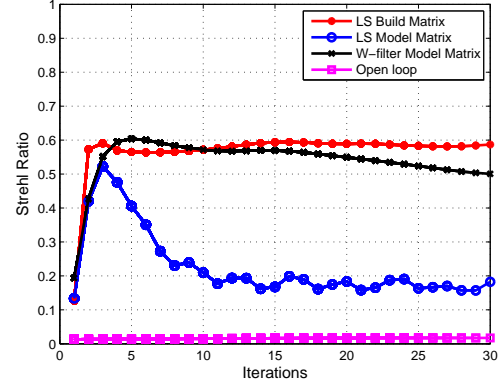
(b) Misregistration $= 30\%$, $f_{3dB}/f_G = 5$
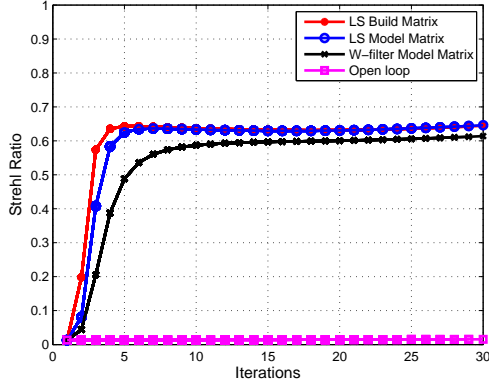
(c) Misregistration $= 5\%$, $f_{3dB}/f_G = 15$
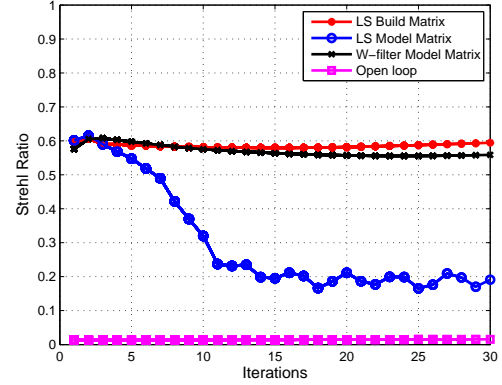
(d) Misregistration $= 30\%$, $f_{3dB}/f_G = 15$

Figure 4.5: This figure gives the results of the 15×15 subaperture AO system using a SH WFS run over 30 iterations. Four different reconstruction matrices are used to calculate the four Strehl ratios on each plot. The four reconstruction matrices are the least-squares build, the least-squares model, the W-filter and open-loop. (a) Shows the matrix having a misregistration of 5% of a subaperture with a $f_{3dB}/f_G = 5$.(b) Shows the matrix having a misregistration of 30% of a subaperture with a $f_{3dB}/f_G = 5$.(c) Shows the matrix having a misregistration of 5% of a subaperture with a $f_{3dB}/f_G = 15$. (d) Shows the matrix having a misregistration of 30% of a subaperture with a $f_{3dB}/f_G = 15$.

Table 4.2: SH WFS Strehl ratio averages for a 15×15 subaperture system

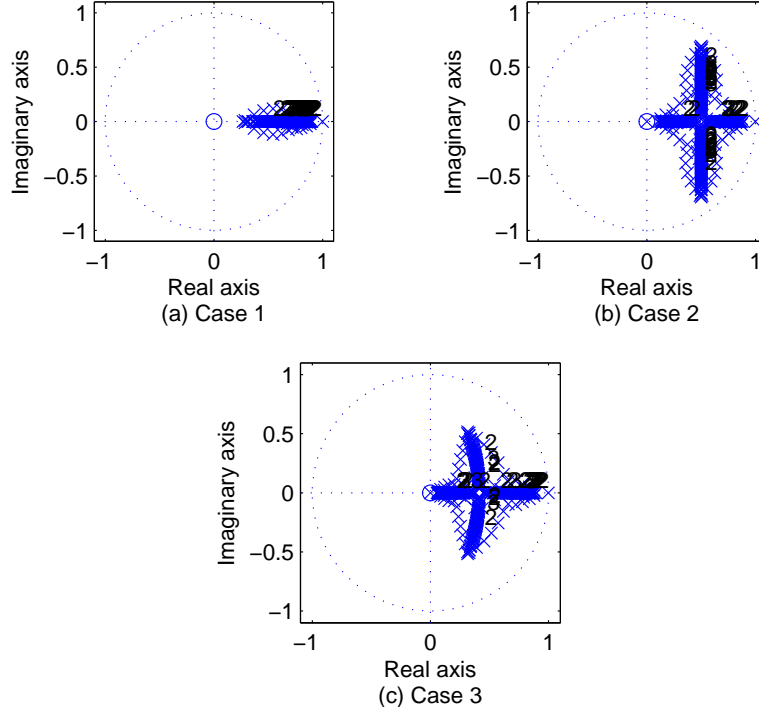| f_{3dB}/f_G	Misregistration %	Build Matrix Strehl Ratio	Model Matrix Strehl Ratio	% Change
2	0%	0.64	0.63	1.3%
	5%	0.62	0.61	1.9%
	15%	0.59	0.57	4.7%
	30%	0.55	0.20	175.9%
	50%	0.43	0.01	12322.9%
5	0%	0.66	0.65	0.29%
	5%	0.65	0.65	0.4%
	15%	0.63	0.61	3.0%
	30%	0.58	0.19	214.4%
	50%	0.41	0.01	5547.2%
10	0%	0.65	0.65	1.1%
	5%	0.65	0.65	0.11%
	15%	0.63	0.62	1.5%
	30%	0.59	0.22	168.0%
	50%	0.35	0.01	4826.8%
15	0%	0.64	0.64	0.11%
	5%	0.63	0.63	-0.05%
	15%	0.62	0.61	1.0%
	30%	0.58	0.27	114.5%
	50%	0.35	0.01	5461.9%

Figure 4.6: SRI closed-loop poles for a 15×15 subapertures, the closed-loop poles are plotted for a misregistration of $\delta = 0.12$ subapertures. The three cases are defined in Eq. (2.34) with solutions in Eq.(3.12). The servo gains were $a = 0.998$ and $b = 0.5$. The Γ matrix was created using the poke method.

4.2 Self-Referencing Interferometer Reconstruction Matrix

4.2.1 Analytical Calculations. Analytical calculations were completed on a general setup for a SRI WFS using the Hudgin geometry as described in Chapter II. Three analytical calculations were completed, and the stability of the AO system was shown with misregistration. Two simulations were set up using the SRI WFS, an 8×8 subaperture system, and a 16×16 subaperture system. Different levels of misregistration were placed on the systems as well as different f_{3dB}/f_G levels.

Figure 4.1 was also compared to Fig. 4.6 which maintains the same parameter of misregistration and gain levels but is now using a SRI WFS. The comparison between the two sets of graphs shows that both maintain stability by having all the
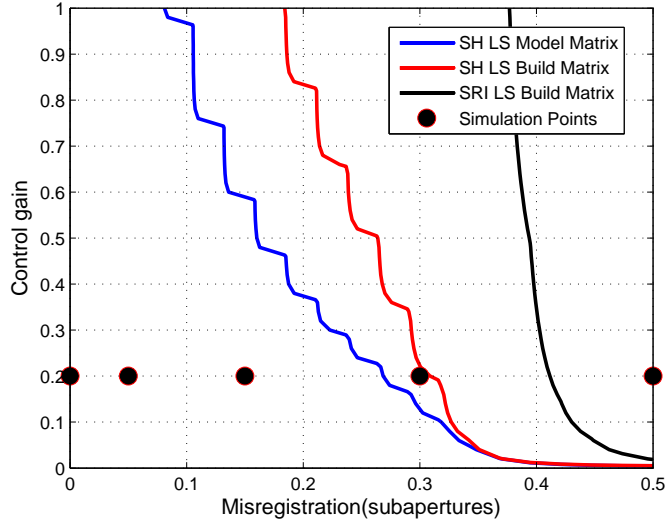
Figure 4.7: Stability lines of a 15×15 subaperture system. This figure illustrates the relationship of instability to misregistration and gain. The area under the curves is the stable region while the area above the curves is the unstable region. The least-squares model matrix refers to a WaveProp build reconstruction matrix, the least-squares build matrix refers to poke build SH reconstruction matrix, and the SRI least-squares build matrix refers to the SRI poke built SRI reconstruction matrix. All used the control law given in Eq. (3.12), Case 1.

poles within the unit circle.

The next test probes the coupling effects of gain and misregistration. In Fig. 4.7 a contour line has been drawn. The graph shows that when the combination of gain and misregistration is at a point below the curve, the system is stable. This graph also shows that the SH built reconstruction matrix (the red curve) has a greater area of stability than the SH model matrix (the blue curve). However, both fall below the SRI built reconstruction (the black curve). This suggests that the SRI should be less sensitive to misregistration than the SH WFS. A comparison to the SRI model matrix was not completed due to the fact that WaveProp does not have a model misregistered matrix for the SRI.
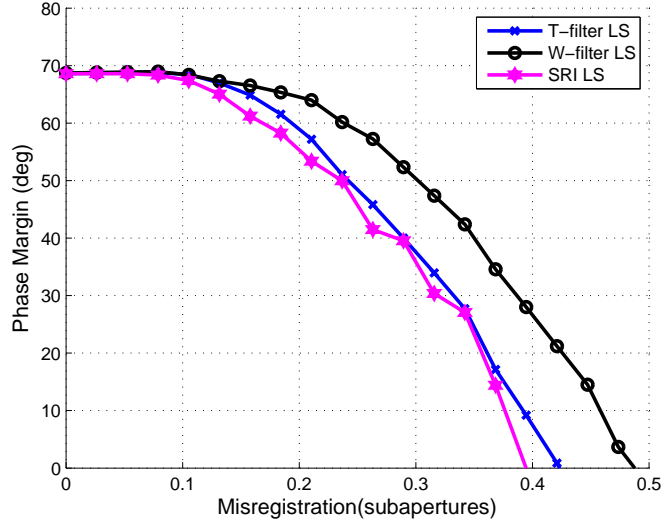
Figure 4.8: Phase margins of a 15×15 subaperture system. This figure illustrates the phase margins that were calculated for misregistration up to half of a subaperture. The build least squares reconstructor was evaluated as well as the T- and W-filters.

The final analytical calculation performed is displayed in Fig. 4.8. This graph shows that the measured reconstructor has similar phase margins as the T- and W-filters. The phase margins of each reconstruction matrix are not degraded much with misregistration until the misregistration reaches 20% of a subaperture.

4.2.2 Simulation Performance. Figure 4.9 gives the Strehl ratios of an 8×8 subaperture AO simulation with a SRI reconstructor. For plot (a) with $f_{3dB}/f_G = 5$ and a misregistration of 5%, the simulations showed that for each reconstruction matrix the Strehl ratios were approximately equal. For the most part, the model matrix outperforms the measured matrix in all the scenarios of the 8×8 subaperture system. This shows the stability of the model matrix and also the need for better design of the measured matrix. In fact for the SRI reconstructor, Table 4.3 shows that even at high misregistration the model matrix performs better. When the number of subapertures is increased to 15×15, the model matrix begins to break down with higher misregistration. This is shown in Fig. 4.10 looking at plots (b) and (d); when

60

Table 4.3:   SRI WFS Strehl ratio averages for a 8×8 subaperture system

| f_{3dB}/f_G	Misregistration %	Build Matrix Strehl Ratio	Model Matrix Strehl Ratio	% Change
2	0%	0.50	0.58	-13.0 %
	5%	0.50	0.55	-10.3 %
	15%	0.47	0.50	-5.0 %
	30%	0.39	0.41	-6.6 %
	50%	0.26	0.27	-3.9 %
5	0%	0.71	0.77	-7.6 %
	5%	0.69	0.73	-6.1 %
	15%	0.64	0.66	-3.8 %
	30%	0.48	0.56	-13.4 %
	50%	0.32	0.34	-6.7 %
10	0%	0.76	0.82	-7.5 %
	5%	0.74	0.79	-6.6 %
	15%	0.68	0.73	-5.9 %
	30%	0.50	0.62	-19.2 %
	50%	0.34	0.39	-13.3 %
15	0%	0.77	0.84	-8.2 %
	5%	0.75	0.81	-7.5 %
	15%	0.70	0.75	-7.4 %
	30%	0.50	0.65	-22.3 %
	50%	0.34	0.42	-19.9 %

the system has 30% misregistration, the model matrix has a strong downward slope. The geometry matrix and the W-filter are maintaining a steady Strehl ratio, especially in (d). This illustrates that, for larger systems, the measured matrix can hold its performance for higher amounts of misregistration. Again, this is the point when the analytical calculations show that the system has reached a point of instability.
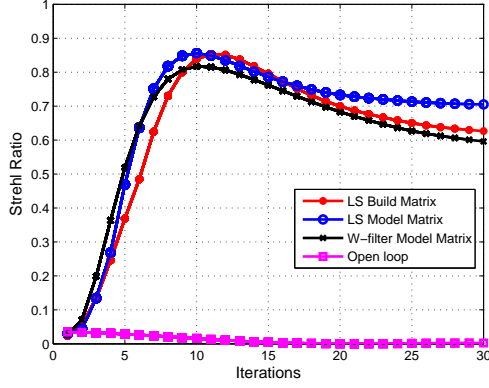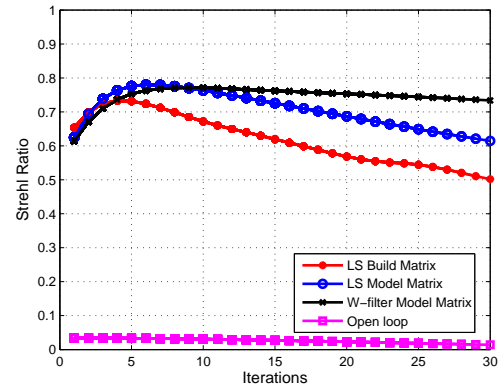
(a) Misregistration = 5%, $f_{3dB}/f_G = 5$
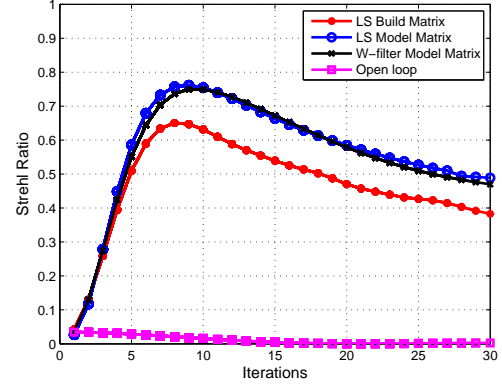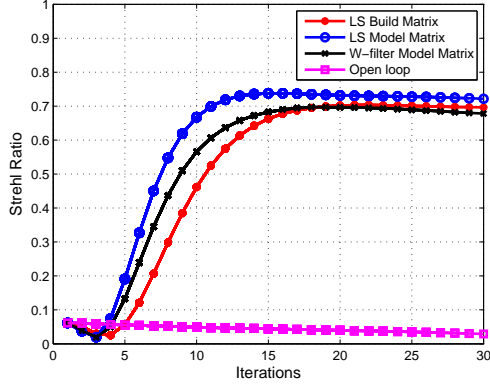
(b) Misregistration = 30%, $f_{3dB}/f_G = 5$
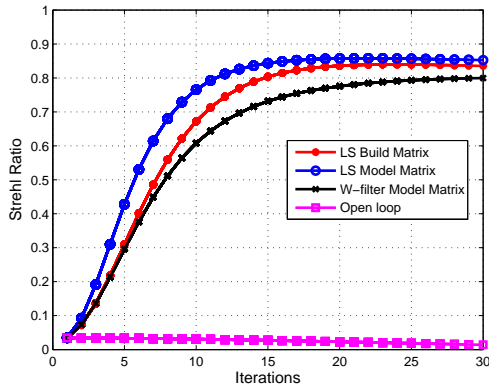
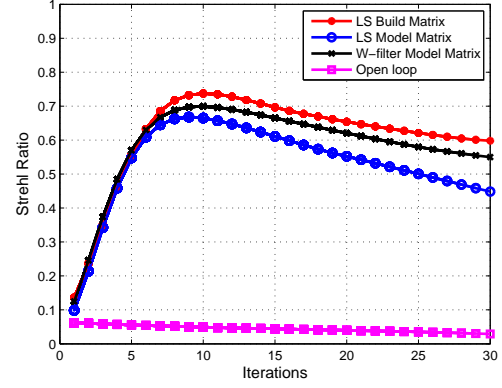(c) Misregistration = 5%, $f_{3dB}/f_G = 15$

(d) Misregistration = 30%, $f_{3dB}/f_G = 15$

Figure 4.9:   This figure gives the results of an 8×8 subaperture AO system using a SRI WFS run over 30 iterations. Four different reconstruction matrices are used to calculate the four Strehl ratios on each plot. The four reconstruction matrices are the least-squares build, the least-squares model, the W-filter, and the open-loop. (a) Shows the matrix having a misregistration of 5% of a subaperture with a $f_{3dB}/f_G = 5$. (b) Shows the matrix having a misregistration of 30% of a subaperture with a $f_{3dB}/f_G = 5$.(c) Shows the matrix having a misregistration of 5% of a subaperture with a $f_{3dB}/f_G = 15$.(d) Shows the matrix having a misregistration of 30% of a subaperture with a $f_{3dB}/f_G = 15$.
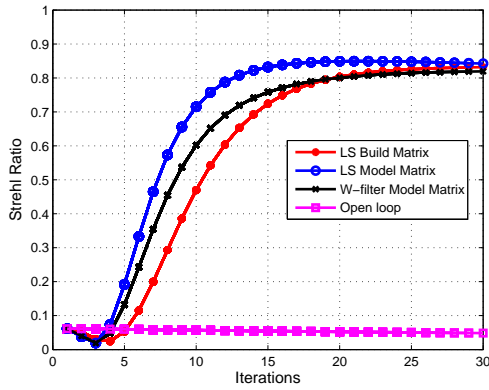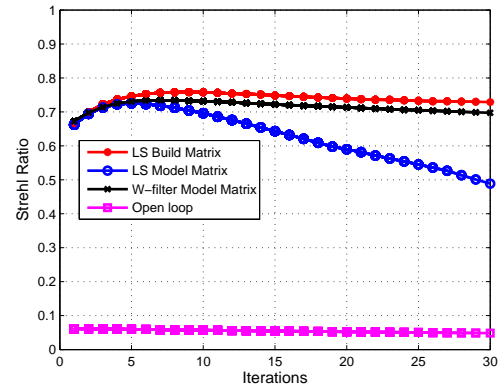
(a) Misregistration = 5%, $f_{3dB}/f_G = 5$ (b) Misregistration = 30%, $f_{3dB}/f_G = 5$

(c) Misregistration = 5%, $f_{3dB}/f_G = 15$ (d) Misregistration = 30%, $f_{3dB}/f_G = 15$

Figure 4.10: This figure gives the results of the 15×15 subaperture AO system using a SRI WFS run over 30 iterations. Four different reconstruction matrices are used to calculate the four Strehl ratios on each plot. The four reconstruction matrices are the least-squares build, the least-squares model, the W-filter and open-loop. (a) Shows the matrix having a misregistration of 5% of a subaperture with a $f_{3dB}/f_G = 5$.(b) Shows the matrix having a misregistration of 30% of a subaperture with a $f_{3dB}/f_G = 5$.(c) Shows the matrix having a misregistration of 5% of a subaperture with a $f_{3dB}/f_G = 15$. (d) Shows the matrix having a misregistration of 30% of a subaperture with a $f_{3dB}/f_G = 15$.

Table 4.4:   SRI WFS Strehl ratio averages for a 15×15 subaperture system

f_{3dB}/f_G	Misregistration %	Build Matrix Strehl Ratio	Model Matrix Strehl Ratio	% Change
2	0%	0.40	0.51	-21.4 %
	5%	0.40	0.49	-18.4 %
	15%	0.38	0.44	-14.4 %
	30%	0.35	0.35	-1.4 %
	50%	0.23	0.20	16.8 %
5	0%	0.67	0.77	-12.2 %
	5%	0.66	0.74	-10.8 %
	15%	0.61	0.69	-11.1 %
	30%	0.59	0.56	6.0 %
	50%	0.40	0.32	26.4 %
10	0 %	0.74	0.84	-12.5 %
	5%	0.72	0.82	-11.7 %
	15%	0.64	0.76	-16.0 %
	30%	0.65	0.63	2.3 %
	50%	0.44	0.38	17.1 %
15	0%	0.75	0.87	-13.5 %
	5%	0.73	0.85	-13.1 %
	15%	0.64	0.79	-19.3 %
	30%	0.65	0.66	-1.5 %
	50%	0.45	0.41	10.6 %

V. Conclusions

This chapter presents a summary of research and some key conclusions from the simulations. It also outlines recommendations for future work.

5.1 Summary

The purposes of this research were to study the effects of misregistration on AO systems and to analyze several means of mitigating it. Misregistration is a constant condition on all AO systems and is always a concern when setting up any experiment. In conducting AO experiments, AFRL's ASALT laboratory seeks to maintain a misregistration of less the 3% of a subaperture. This precision is necessary both to validate their research and to afford them the ability to repeat the process. Currently, this restriction requires highly trained engineers and very precise alignment procedures. However, in the field the AO system must be capable of performing at a high standard, and the time and talent to register the system to these exacting standards are not always available. Mitigation strategies must therefore be developed in order to maintain high performance with greater amounts of misregistration, especially when the misregistration is dynamically introduced by platform vibrations.

Specifically, this research studies how misregistration would affect a SH WFS differently than a SRI WFS. This research explored some of the differences between the reconstruction methods of a SH WFS and a SRI WFS. The same analysis was performed for each WFS, in order to estimate when each system would become unstable. Different mitigation strategies were examined, and a poke method was introduced. The mitigation strategy of using a unique reconstructor built using the WFS measurements was developed and tested for both the SH and SRI AO systems. The built reconstructor was compared against the model matrix used in most traditional AO settings. The simulations showed that for larger AO systems, the built matrix maintained the performance levels better than did the model matrix. Also, even with

up to 50% misregistration, the built matrix showed much less system performance degradation than the model matrix.

5.2 Conclusions

It can be generally concluded that the introduction of the measured reconstruction matrix usually improved the systems' performance when there was a large amount of misregistration. Many things were learned from the result of this research. The main points taken from the research are that

- the measured matrix analytically shows a greater amount of resistance to instability due to misregistration,

- the smaller systems display better performance with the model matrix with misregistration than the larger systems,

- the poke matrix has a greater impact on the larger system to maintain stability and high performance when there is misregistration,

- the phase margin of the build SRI matrix predicted the higher resistance to instability with misregistration on the system,

- analytic calculations predict that the SRI WFS is less sensitive to misregistration than the SH WFS.

In summary, the design of a new reconstruction matrix using the measurements of the WFS was a success; the strongest showing was with the larger systems. This research shows that with the larger systems, the potential of correcting misregistration by constructing a unique poke matrix is a viable method. More work needs to be done to improve the performance of the system.

5.3 Recommendations

This research was limited in its scope to four very simple cases with very little real-world distortion to hinder the process. The next step would be to simulate a real-world AO system with noise, slaves, and a circular aperture. Also, it is shown that

bigger AO systems perform better with the measured matrix, so subsequent research should increase the size of the AO system to discover if this trend continues. Another direction this research could take would be to study the combination of mitigation strategies. The use of the W-filter showed very solid results, so the combination of the build matrix and W-filter has strong possibilities of improving performance and stability. The phase margins and stability of the simulation could be analyzed to gain a more direct comparison with the analytic calculations. Finally, the process should be tested on a real AO system so it could be studied experimentally.

Bibliography

1. Andrews, Larry C. and Ronald L. Phillips. *Laser Beam Propagation through Random Media.* SPIE Press, 2nd edition, 2005.

2. Brennan, Terry J. *Hartmann Sensor Misregistration: Stability and Stability Margins.* Technical Report 1426, The Optical Sciences Company, August 1998.

3. Brennan, Terry J. *The Use of Spatial Filtering Techniques to Reduce ABL Stability Margin Loss.* Technical Report 1450, The Optical Sciences Company, April 1999.

4. Brennan, Terry J., Phillip H. Roberts, and David C. Zimmerman. *WaveProp A Wave Optics Simulation System For Use with* `Matlab`® . The Optical Sciences Company, 1.07 edition, 2008.

5. Gavel, Donald. "Suppressing Anomalous Localized Waffle Behavior in Least Squares Wavefront Reconstrutors". volume 4839, 972–980. SPIE, 2003.

6. Goodman, Joseph W. *Introduction to Fourier Optics.* Roberts & Company, 3rd edition, 2005.

7. Hardy, J. W. *Adaptive Optics for Astronomical Telescopes.* Oxford University Press, 1998.

8. Hecht, Eugene. *Optics.* Pearson Education, 4th edition, 2002.

9. Hyde, Milo, Michael Dulski, and Nathan Engstrom. "High Order Wavefrontsensor Measurements", 2008. Air Force Institute of Technology.

10. Lukin, Vladimir P. and Boris V. Fortes. *Adaptive Beaming and Imaging in the Turbulent Atmosphere.* SPIE Press, 2002.

11. Penrose, R.A. "Generalized Inverse for Matrices". volume 51, 406–413. Proc.Cambridge Phil. Soc., 1955.

12. Rhoadarmer, Troy A. "Development of a self-referencing interferometer wavefront sensor". *SPIE*, 5553, 2004.

13. Rhoadarmer, Troy A. and Laura M. Klein. "Design of a spatially phase shifted self-refencing interferometer wave front sensor". *SPIE*, 6306, 2006.

14. Schmidt, Jason D. "Wave Optics I, class notes", Spring 2008. Air Force Institute of Technology.

15. Schmidt, Jason D. "Imaging Through Turbulence, class notes", Summer 2008. Air Force Institute of Technology.

16. Tyson, Robert K. *Introduction to Adaptive Optics.* SPIE Press, 2000.

17. Vitayaudom, Kevin P. *Analysis of Non-Uniform Gain for Control of a Deformable Mirror in an Adaptive-Optics System.* Master's thesis, AFIT, 2008.

REPORT DOCUMENTATION PAGE

1. REPORT DATE *(DD–MM–YYYY)*	2. REPORT TYPE		3. DATES COVERED *(From — To)*
17–03–2009	Master's Thesis		Aug 2007 — Mar 2009

4. TITLE AND SUBTITLE	5a. CONTRACT NUMBER
Misregistration in Adaptive Optics Systems	
	5b. GRANT NUMBER
	F2KBAC8308G001
	5c. PROGRAM ELEMENT NUMBER

6. AUTHOR(S)	5d. PROJECT NUMBER
	ENG JON 145
Engstrom, Nathan D., Capt, USAF	**5e. TASK NUMBER**
	5f. WORK UNIT NUMBER

7. PERFORMING ORGANIZATION NAME(S) AND ADDRESS(ES)	8. PERFORMING ORGANIZATION REPORT NUMBER
Air Force Institute of Technology	
Graduate School of Engineering and Management (AFIT/EN)	
2950 Hobson Way	AFIT/GE/ENG/09-14
WPAFB OH 45433-7765	

9. SPONSORING / MONITORING AGENCY NAME(S) AND ADDRESS(ES)	10. SPONSOR/MONITOR'S ACRONYM(S)
Air Force Research Laboratory	AFRL/RDS
Darryl J. Sanchez, PhD	
3550 Aberdeen Ave SE	**11. SPONSOR/MONITOR'S REPORT NUMBER(S)**
Kirtland Air Force Base, NM 87117-5776	
(505) 846-7209 (DSN:246-7209), email: darryl.sanchez@kirtland.af.mil	

12. DISTRIBUTION / AVAILABILITY STATEMENT

Approved for public release; distribution is unlimited.

13. SUPPLEMENTARY NOTES

14. ABSTRACT

An adaptive optics (AO) system is most effective when there is a known alignment between the wave front sensor (WFS) and the deformable mirror (DM). Misregistration is the term for the unknown alignment between the WFS and DM. Misregistration degrades system performance and can make the system unstable. An AO system uses a reconstruction matrix to transform WFS measurements into DM commands. A standard AO system uses a model reconstruction matrix that assumes perfect registration between the WFS and DM. The object of this research is to mitigate the negative effects of misregistration by using offline WFS measurements to create the reconstruction matrix. To build the reconstruction matrix, each actuator on the DM is poked to a fixed amount, and then the resulting measurement on the WFS is recorded. Analytic studies of the model and measured matrices show that the measured matrix yields a more stable AO system. Additional simulations indicate that applying the measured matrix improves the overall system performance compared to that of the model reconstruction matrix.

15. SUBJECT TERMS

misregistration, adaptive optics, reconstruction matrix

16. SECURITY CLASSIFICATION OF:			17. LIMITATION OF ABSTRACT	18. NUMBER OF PAGES	19a. NAME OF RESPONSIBLE PERSON
a. REPORT	b. ABSTRACT	c. THIS PAGE			Maj Jason D. Schmidt, PhD AFIT/ENG
U	U	U	UU	79	**19b. TELEPHONE NUMBER** *(include area code)* (937) 255–3636, ext 7224; jschmidt@ afit.edu